POLITECNICO DI TORINO

Collegio di Ingegneria Meccanica, Aerospaziale, dell'Autoveicolo e della Produzione

Corso di Laurea Magistrale
in Ingegneria Meccanica

Tesi di Laurea Magistrale

Modelling of diesel particulate filtration in wall-flow traps based on generic channel geometry approach

Supervisor
Prof. Samir Bensaid

Hosting University Supervisor:
Prof. Miguel Abreu Almeida Mendes

Candidate

Antonio Maione

Anno Accademico 2017-2018

Alla mia famiglia.

Abstract

Although diesel engines offer higher thermal efficiency, lower fuel consumption and lower HC pollutant emissions, larger amounts of NO_x and PM are emitted compared with equivalent gasoline engines. The diesel particulate filters (DPFs) have proved to be one of the most promising after-treatment technologies due to the more stringent particulate matters (PM) regulations.

The estimation of the PM mass accumulated in DPF and total pressure drop across the filter are very important in order to determine when carrying out the active regeneration of the DPF. The study numerically evaluates the filtration process of several DPF geometries, taking into account some already offered geometries and others not yet commercialized. The investigated designs are: square/square, triangular/triangular, hexagon/triangle, octagon/square and hexagon/hexagon.
Firstly the numerical model is analyzed, highlighting the multi-scale length of the model and the generic channel geometry approach. Furthermore, it is deeply explained a method used to obtain asymmetric geometries by changing the wall thickness distribution to inlet and outlet channels of the DPF. This method leads to the investigation of many geometries with different geometrical relationships.
Besides the validation of the model with some experimental investigations proposed in literature, two exhaust gas conditions are analyzed. Several geometries are studied according to these exhaust gas conditions, comparing the results in terms of pressure drop, PM mass accumulated and efficiency of the DPF.
A generic channel geometry study is provided in order to understand the effectiveness of the already investigated geometries; in addition, it could examine if better solutions are admissible for the cases under exam. This final analysis researches an eventual criterion to previously identify if a specific geometry could offer consistent and satisfying results.

Acknowledgements

I would like to thank my thesis hosting university advisor prof. Miguel A. A. Mendes of LASEF, the Laboratory of Simulation in Energy and Fluids, at Instituto Superior Técnico of Lisbon. He has always been available and friendly during our working days in Lisbon. He constantly helped me, from the first day until my last day in Portugal, providing suggestions for the analysis, scientific articles to better understand the subject, recommendations for the future and also travel tips for visiting Portugal. I would also like to thank all the others members of LASEF, that helped me to understand the models and the new software that I had never used before.

I would also like to thank professor Samir Bensaid of Politecnico di Torino. As the reference professor of my thesis in Italy, he gave many suggestions when involved in the project. Furthermore, once I came back to Italy, he supported my work providing some other improvements.

Moreover, I thank my family, always supporting me during the difficult and long university years. They encouraged me even before my first day at Politecnico di Torino, constantly giving me the courage to move on. I deeply acknowledge Paola, giving the same passion, attention and importance to me, encouraging all my life choices. She has been so important in my academic path to be an integral part of this work as well as of my academic results.

Furthermore, I would like to acknowledge my old friends Biagio, Gianluigi and Salvatore, being constantly part of my life during my academic years. I acknowledge my friend Marialaura C. and Mario, Marialaura T., Laura and all my friends from my island that have donated their support during these five years. And last but not least, I sincerely thank my friends in Turin, the Neapolitan group (Alessandro, Bruno, Francesco, Gianluca Manuel and Mattia), the Ischian group (Francesco, Gianluca, Luca and Michele) and all my old academic colleagues.

Contents

List of Figures

List of Tables

Nomenclature

ϵ Porosity

μ_{gas} Gas dynamic viscosity (Pa$\times s$)

ϕ_{d} Ratio of deposit density to particle density

ρ_d Deposit density (kg/m^3)

$\rho_{soot,c}$ Cake packing density (kg/m^3)

ρ_s Cake density (kg/m^3)

A_{01} Clean filter inlet cross-section area (m^2)

A_{02} Clean filter outlet cross-section area (m^2)

A_e Periodic element area (m)

$CPSI$ Cell per square inch (in^{-2})

d_{pore} Wall pore diameter (m)

f_1 Fraction of wall to inlet channel

K_w Filter wall permeability (m^2)

K_0 Clean filter permeability (m^2)

K_s Cake permeability (m^2)

l Channel length (m)

l_s Local cake thickness (m)

M_{gas} Molar mass (kg/mol)

P_{01} Clean filter inlet cross-section perimeter (m)

P_{02} Clean filter outlet cross-section perimeter (m)

p_{out} Channel outlet pressure (Pa)

P_w Clean filter wall cross-section perimeter (m)

r_{120} Ratio of inlet channel area to outlet channel area (neglecting filter wall)

r_{12} Ratio of inlet channel area to outlet channel area

r_{wp0} Ratio of the inlet perimeter to square root of area of the element (neglecting filter wall)

r_{wp} Ratio of the inlet perimeter to square root of area of the element

T_{gas} Temperature of the gas at the DPF intake (K or °C)

t_{wall} Wall thickness (m)

u_w Gas through-wall velocity (m/s)

v_{appr} Cross sectional velocity of the filter (m/s)

CPSC Cells per square centimeter (cm^{-2})

Introduction

1.1 Diesel engine emissions

The typical diesel engine is an auto-ignition engine in which fuel and air are mixed inside the engine. The air required for combustion is compressed inside the combustion chamber. Consequently to the injection of diesel fuel, the mixture ignites spontaneously. This event happens due to the high temperature developed during the process. Not differently from the other main fossil fuel, diesel fuel is mainly composed of carbon and hydrogen. The ideal oxidation of the fuel would only generate CO_2 and H_2O.

However, there are many reasons (the air-fuel ratio, ignition timing, turbulence in the combustion chamber, combustion form, air–fuel concentration, combustion temperature, etc.) why the ideal products are not obtained. This leads to the generation of harmful combustion products like: CO, HC, NO_x, and PM. Figure 1.1 shows a typical composition of diesel exhaust gas. Pollutant emissions are only less than 1 % of the exhaust gas. The distribution of these gases is not uniform: NO_x has a rate of more than 50 %. After NO_x emissions, PM has the second highest proportion in pollutant emissions. Furthermore, there is a small fraction of SO_2 depending on specifications and quality of fuel.
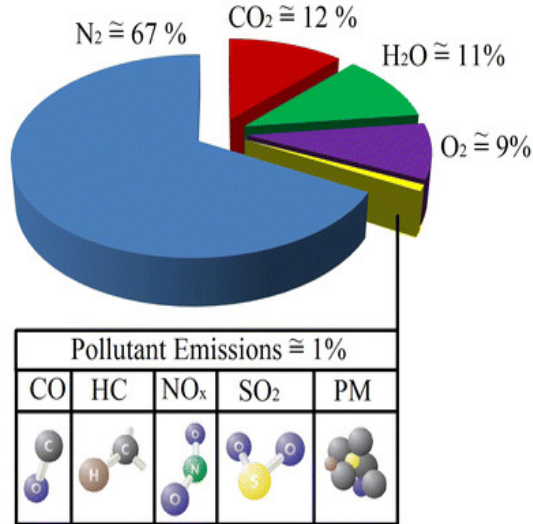
Figure 1.1: Compositions of diesel exhaust gas (1).

Diesel particulate matter (DPM or PM for this work) mainly comes from the carbon of the fuel (48%), while the other compounds come from lubricant oil (25%), sulfates (14%) and ash (13%). PM is mainly composed of two kinds of particles:

1. solid particle (soot);

2. organic component with high molecular mass (Soluble Organic Fraction: SOF).

Soot is composed of carbonous particles (results of incomplete combustion of the hydrocarbons) and ash. The latter particles are not burnt anymore during after-treatment processes. This lead to accumulation problems described in Section 1.2.3.

Diesel pollutants are often emitted close to where people live or permanently work. The emissions are released at ground level and are suspended in the air. The pollutants get into our bodies when we breathe. Some of the PM is large enough to be visible as smoke, while most are in the invisible sub-micrometer range. Particles differ in size, composition, solubility and therefore also in their toxic properties. Diesel exhaust contains a variety of confirmed carcinogenic compounds such as formaldehyde, acetaldehyde, dioxins and polycyclic aromatic hydrocarbons (PAHs). Over 30 epidemiological studies link diesel exhaust to lung cancers.

Furthermore, diesel soot emissions contribute to the development of pollution of air, water, and soil; soiling of buildings; reductions in visibility; impact agriculture productivity, global climate change (9).

1.2   Diesel particulate filter

The PM (particulate matter) emission of Diesel engines has been faced thanks to the development of DPFs (Diesel Particulate Filters) during the last and the present century (it was equipped for the first time in 1985). Year by year the quality and the efficiency of DPFs improved, changing from a non-regeneration action to the actual two main ways to realize the regeneration (10). With the development and the renewal of the emission standards (e.g. EURO VI in Europe), the control of soot emission has become of central importance. As reported by The European Parliament (Directive 2016/2284 (11)) "sulfur dioxide emissions were reduced by 82 %, nitrogen oxides emissions by 47 %, non-methane volatile organic compounds emissions by 56 % and ammonia emissions by 28 % in the Union between 1990 and 2010. As regards the year 2020 and thereafter, the revised Gothenburg Protocol sets out new emission reduction commitments, taking the year 2005 as a base year, for each party regarding sulfur dioxide, nitrogen oxides, non-methane volatile organic compounds, ammonia and fine particulate matter". Nowadays, PM control can be done using wall-flow diesel particulate filters (DPFs) (8), they have become the most effective technology for the control of diesel particulate emissions - including particle mass and numbers - with high efficiencies (5). It has been improved the mechanical and thermal durability of the filter as well as the efficiency of the functional principles of the filters, due to the developments of new technologies.

Since 2007, a growing number of national governments have implemented tailpipe emissions standards that can be met only with the installation of a wall-flow diesel particulate filter (DPF) when applied to diesel engines. These "soot-free" engines — which we define as those equivalent to or better than Euro VI for HDVs, Euro 5b for light-duty vehicles (LDVs), or any policies that explicitly require the installation of a DPF — are capable of reducing exhaust emissions of diesel BC by 99% compared with older-technology engines. Implementation of these limits also requires improvements in diesel fuel quality to no greater than 10–15 parts per million (ppm) of sulfur for soot-free engines to operate most effectively. Most of the world's diesel supplier by volume are already adequate to fuel vehicles meeting Euro VI-equivalent emissions standards. As of 2018, more than 70% of the world's road diesel is ultralow-sulfur. Under policies adopted as of May 2018, this share is projected to grow to more than 80% by 2021. Yet at least 127 countries still have average

on-road diesel sulfur levels above 15 ppm. Particularly for heavy-duty diesel trucks and buses, securing cleaner fuels is a critical milestone for achieving deep reductions in BC (black carbon) emissions (2).

According to Miller et al. (2), 40% of new heavy-duty diesel vehicles (HDDVs) sold worldwide are equipped with DPFs . This share is projected to grow to 50% in 2021 after adopted Euro VI-equivalent standards have gone into force in India and Mexico. If China and Brazil introduce Euro VI-equivalent standards, the share of new HDDVs with DPFs would increase to 70% (see Figure 1.2).
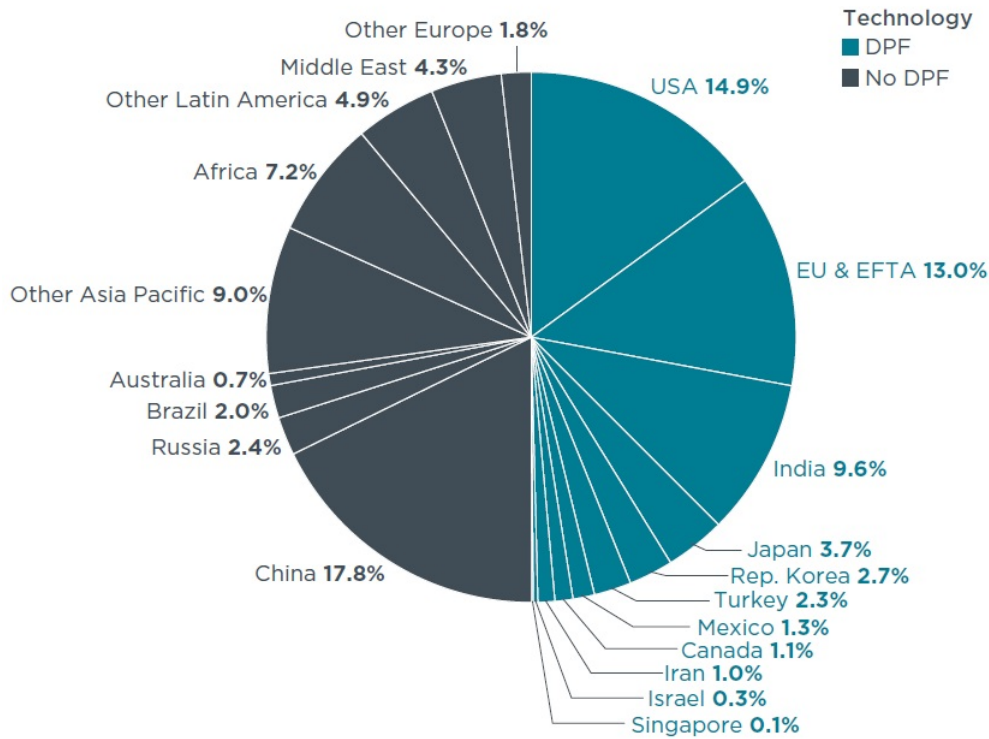
Figure 1.2: Share of global new heavy-duty diesel vehicle sales with diesel particulate filters under adopted policies in 2021 (2).

While soot-free standards are increasing the share of new vehicles equipped with DPFs, the transition will take substantially longer for the in-use vehicle fleet to turn over and be replaced with cleaner vehicles. In 2012, 5% of in-use HDDVs were equipped with DPFs. This share tripled by 2018 to 15%. Under currently adopted policies, one in five in-use HDDVs worldwide will have a DPF by 2021 (see Figure 1.3).

% of new heavy-duty diesel vehicle sales

| 2012 | 2015 | 2018 | 2021 |

% of heavy-duty diesel vehicle stock

| 2012 | 2015 | 2018 | 2021 |

Technology ■ DPF ■ No DPF
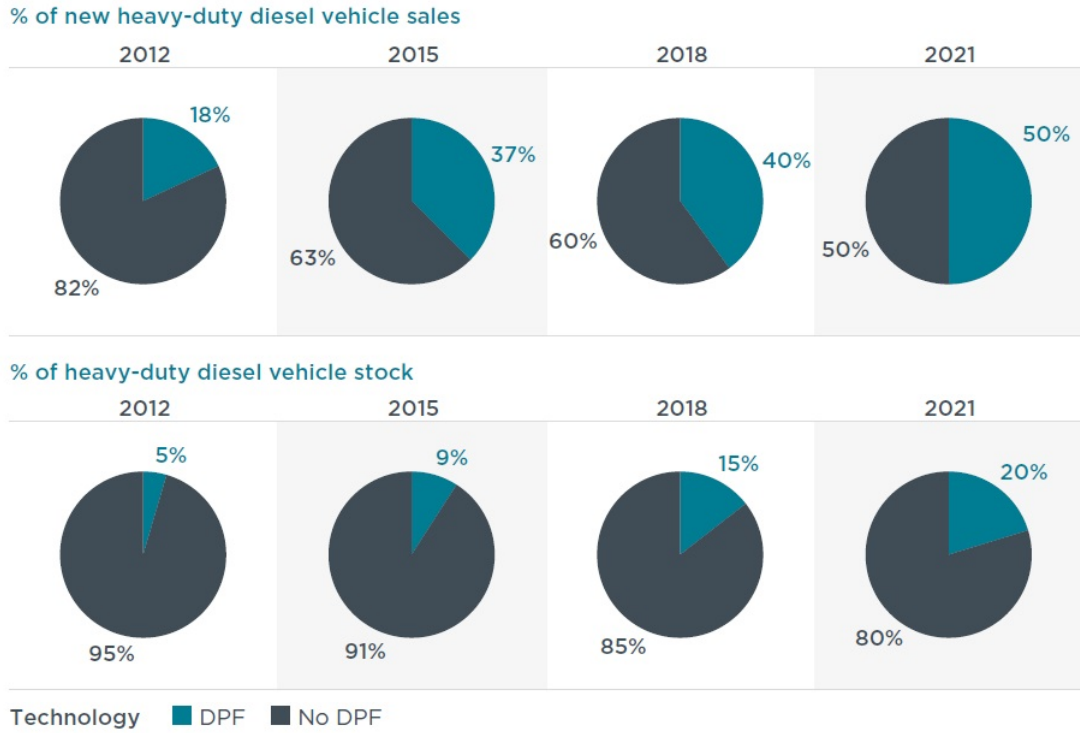
Figure 1.3: Share of global heavy-duty diesel vehicle sales and stock equipped with diesel particulate filters (2).

1.2.1 Filter composition

The common design of a diesel particulate filter is a wall-flow monolith, extruded with a cylindrical structure. The surfaces are composed by several parallel channels along the axial direction. Different from a common flow-through filter, DPFs are composed by wall-flow filter where the flow is forced to pass through the wall of the filters and not through the channels of the filters. In Figure 1.4-1.5 the different filtration mechanism between a wall-flow filter and a flow-through filter is shown either in terms of flowing mechanism (Figure 1.4) either in terms of design aspect (Figure 1.5).
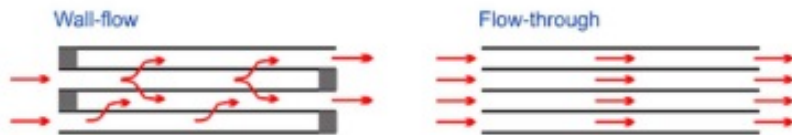
Figure 1.4: Differences flowing of the gas between
wall-flow and flow-through filters (3).
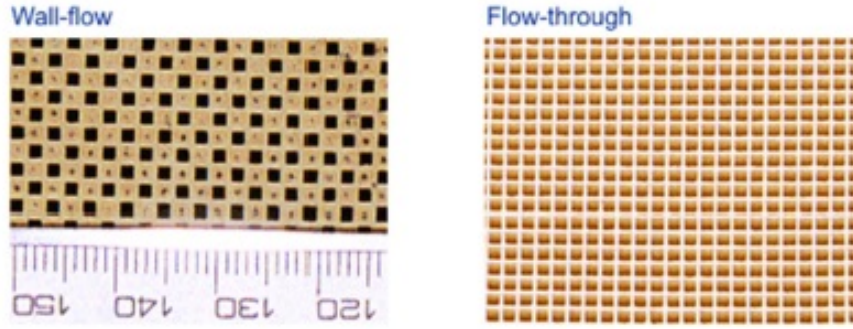
Figure 1.5: Design differences between wall-flow and
flow-through filters (3).

1.2.2 Filtration mechanisms

Filtration in DPFs is manly composed by two different phases (8; 6).

1. *Depth filtration*, where the soot particles are deposited within the filter wall, mainly due to the mechanisms of interception and Brownian diffusion;

2. *Cake formation*, which occurs after the maximum packing density is reached at the inlet region of porous wall and hence, the soot particles are forced to form a compact particulate layer (named as filter cake) on the top of the filter wall.

Figure 1.6 shows the two filtration mechanisms from a microscopic point of view, while in Figure 1.7 shows the typical curve (pressure drop against collected mass) with the transition from deep bed filtration to cake formation.
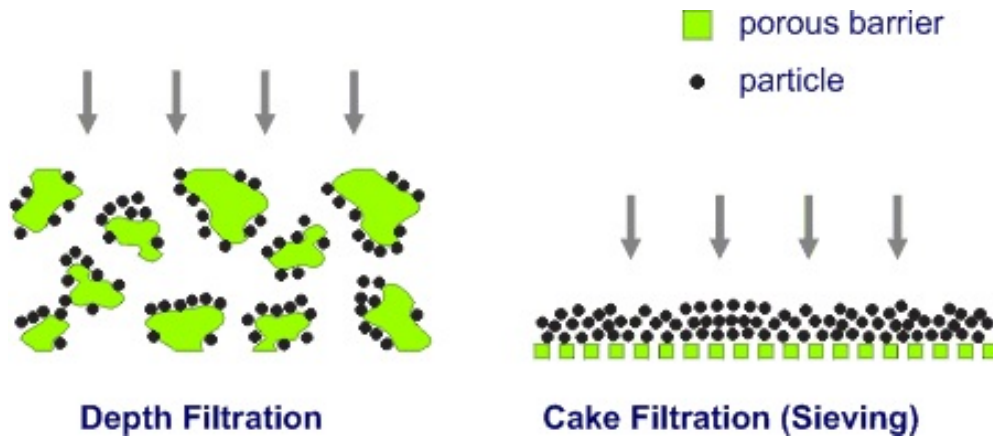
Figure 1.6: Types of filtration (3).
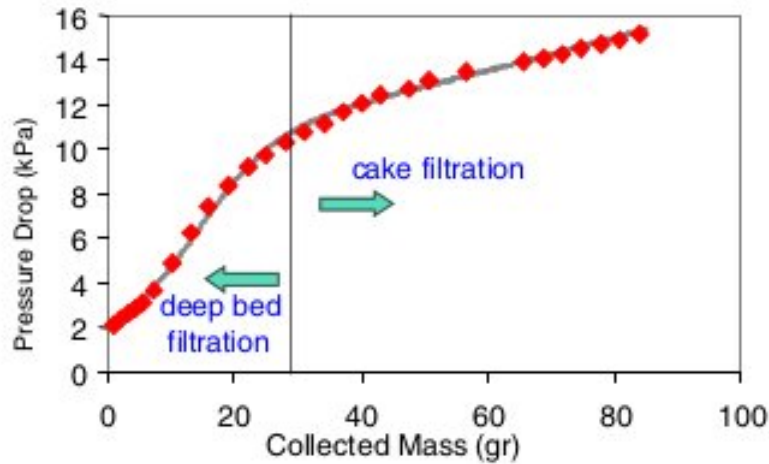
Figure 1.7: Filtration mechanisms example (4).

1.2.3   Regeneration

After the collecting transition of the process, the aim of the filter it to remove the soot particle collected in the trap. While particles are collected across the filter, it is established a pressure drop in the exhaust system, this could affect the engine operation. The technique nowadays used to remove these particles is called regeneration of the filter. It consists of an oxidation of these particles. Regeneration requires temperatures in excess of 550 °C, this value of temperature does not occur often in a diesel engine, especially in light-duty application. The main objective of the regeneration is to be fast and reliable, removing as much as possible all the accumulated particles mass before the back-pressure rises to unacceptably high levels (6). There are two main approaches to regenerate a DPF: active regeneration and passive regeneration. In Figure 1.8 a filter classification is provided depending on the regeneration method.

- In an active regeneration, particulate matter is oxidized periodically according to specific strategies. It depends usually on the load capability of the filter, the pressure drop obtained by the filter and the potential heating supplied by the engine (9). Typically a computer monitors one or more sensors that measure back pressure and/or temperature, and ,based on pre-programmed set points, the computer makes decisions on when to activate the regeneration cycle. The additional fuel can be supplied by a metering pump. The on-board control unit should run the regeneration avoiding excessive fuel consumption but also taking into account eventual engine problems due to high pressure drop across the filter;

- in a passive regeneration, the soot is oxidized thanks to a self-regeneration occurring at the exhaust gas temperature. The soot oxidation temperature is lowered to a level allowing for auto-regeneration during regular vehicle operation - a task commonly achieved by introducing an oxidation catalyst to the system. In this way, the exhaust gasses temperature promotes an ongoing catalytic reaction process (5). There is no extra fuel consumption and it is neither managed by the vehicle operator neither the vehicle engine management system (9).
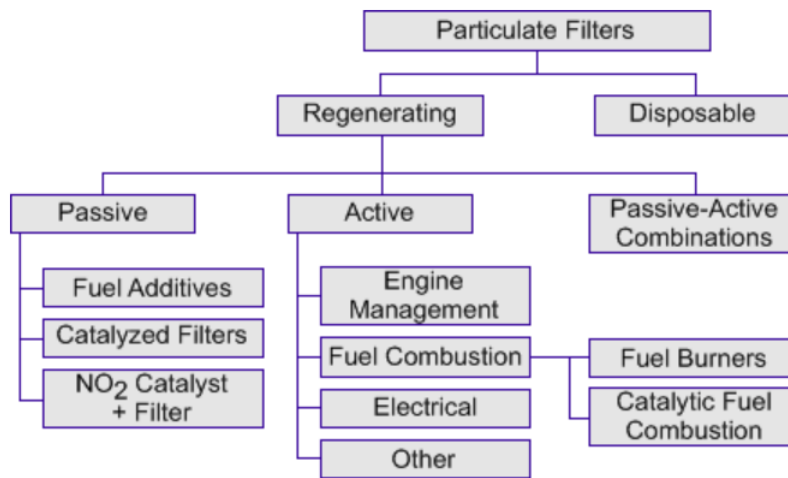
Figure 1.8: Classification of filter systems by regeneration method (5).

Particulate filters also capture inorganic ash particles as part of PM. These incombustible particles cannot be removed from the filter using a thermal regeneration. The accumulation of ash causes a gradual increase of the pressure drop in the filter over its lifespan. Filters can be cleaned from ashes only through dedicated maintenance procedures. The cleaning frequency is typically not more than once per year.

1.2.4 Filter material

The filter material is a key component of the diesel particulate filter system, affecting both its performance and durability. Its task is to physically capture solid particulates and hold them until they can be removed during the regeneration process (periodic or continuous). Furthermore, it has to be resistant to the periodic thermal process occurring during the regeneration phase. In fact, depending on the regeneration method,

diesel filter materials may be exposed to very high temperatures, significantly in excess of 1000°C, as well as rapid temperature changes. These thermal conditions are caused by the release of heat during rapid oxidation of soot accumulated in the filter (regeneration phase). Since the distribution of soot is not necessarily uniform throughout the filter, thermal stress frequently has a local character. Thermal phenomena, both high temperature and thermal stress, are responsible for the majority of filter failures, such as melting or cracking. The reactivity of the filter material with the accumulated ash is another important aspect concerning the filter material. These ashes can either chemically attack and corrode the filter media through solid-state reactions (e.g., creating pinholes) or form eutectic-type systems, which may result in dramatic deterioration of the material melting point (5). Typical reactions of ash related to the in-filter temperature are illustrated in Figure 1.9.
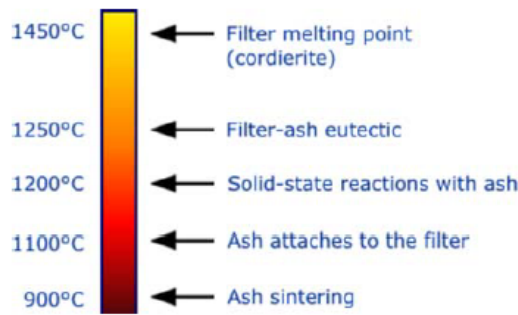
Figure 1.9: Ash reaction in particulate filter (5).

Ceramic wall-flow monoliths are the most common type of diesel filter material. They are utilized in the majority of commercial diesel filter systems, as well as in numerous research and demonstration projects. Monolithic filters, derived from flow-through supports used for automotive catalytic converters, were developed by Corning in cooperation with partners from the automotive industry (12). Monolithic filters are made of cordierite—a synthetic ceramic composition. Cordierite is characterized by very low thermal expansion coefficient, which makes the material resistant to extreme thermal cycling. It also exhibits high-temperature resistance (1200 °C) and good mechanical strength. Wall-flow monoliths are also made of silicon carbide, SiC. Silicon carbide is characterized by better temperature resistance (1800 °C) than cordierite. Its drawback is higher thermal expansion coefficient and higher cost (5). In 2005 it was introduced aluminum titanate-based DPF material, especially for applications in light-duty vehicles. The material is composed of approx. 70%

aluminum titanate and contains Ca/Sr feldspar and mullite. The properties include outstanding thermal shock characteristics, high-temperature stability and chemical stability, but an even lower mechanical strength than that of cordierite. The filters have been used in passenger cars since around 2007 with asymmetric cells (asymmetric cell technology). Thanks to analogous optimization to that carried out for cordierite, specialized materials with improved backpressure or soot mass limit are now available (13).

1.3 Diesel particulate filter design simulation

DPF has been studied for many years. Nowadays the experimental approach it is used only in advanced progression stage of DPFs validation, the recent advanced simulation technology is being consistent and appropriate to predict the DPF phenomena. Traditional experiment approach is very time-consuming and costly, this provides the opportunity to increase and study the power of the simulations. DPF behavior depends on the coupling of physics-chemical phenomena occurring over spatial and temporal scales. Many numerical models were developed over time, admitting different level of complexity (14; 15; 6), as shown in Figure 1.10. There are three main length scales taken into account for the modelling of DPFs (16):

- *Micro-scale models*, where the filtration process along the particulate layer and the porous wall is simulated taking into account the detailed morphology of the solid regions (17). These models may track individual particles using a Lagrangian approach (17) or, alternatively, treat the particles as an interpenetrating continuous phase based on a Eulerian approach (18), and are computationally very expensive for simulating even a small portion of a single filter channel. Therefore, they are rather used to provide closure expressions or correlations required by the meso-scale and macro-scale models.

- *Meso-scale models*, where the particle deposition on the porous wall and subsequent cake formation along the surface of filter channels can be simulated using either a Lagrangian approach (19) or a Eulerian approach (14) for the particles; although the Eulerian approach is computationally cheaper since it replaces the tracking of individual particles with the transport of a representative particle

concentration variable. Additionally, the porous wall is treated as a homogeneous equivalent medium with effective filtration characteristics that can be provided from a micro-scale model, or alternatively from experiments.

- *Macro-scale models*, where the filtration phenomena at the scale of the complete filter are simulated using simplified models (6), which in principle can be derived from the meso-scale models by applying some sort of simplification technique (dimensionality reduction, homogenization approach, etc.). This class of macroscopic models is computationally very cheap and is generally applied for investigating the phenomenological behavior of complete filters, neglecting possible inhomogeneities that may exist inside of them.
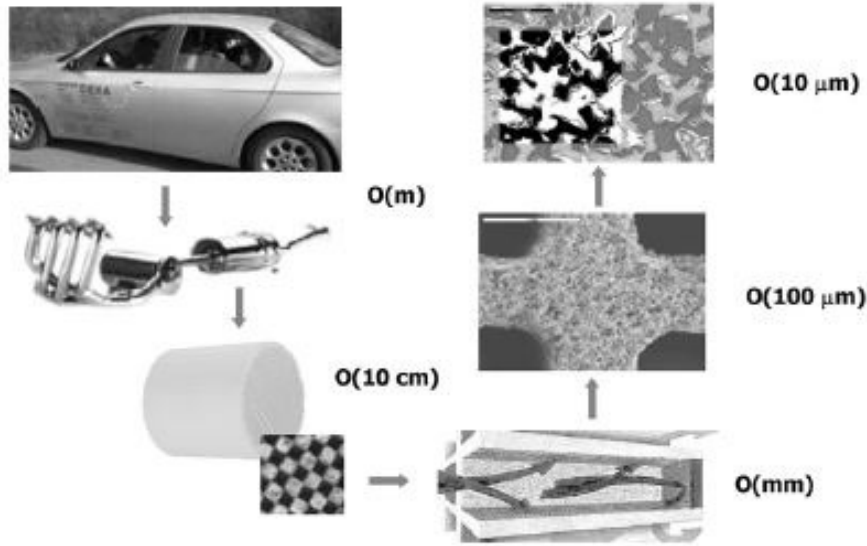
Figure 1.10: DPF simulation scales (6).

In general, meso-scale models offer a good compromise between accuracy and computational effort. For example, Bensaid et al. (14) used a meso-scale model in order to predict the soot deposition distribution inside DPF under different operating conditions, considering a periodic element of the filter comprising only four channels (two inlet and two outlet channels). They adopted a Eulerian approach and numerically solved the 3D governing equations for both the isothermal fluid flow and transport of soot particles, treating the particulate phase as an interpenetrating continuous phase of negligible volume fraction compared to that of the fluid phase. The porous wall of the filter was treated as a homogeneous medium with effective properties and the depth filtration

of particles inside the wall was modeled based on the unit-collector theory (20). They discretized the computational domain using a large non-uniform mesh with approximately 3×10^5 cells and a substantial fraction of the computational effort was devoted to the calculation of the filtration process at the filter wall. Their predictions showed that the flow field inside the filter is highly responsible for the soot deposit distribution along the filter channels and, as the filtration process evolves, the gas through-wall velocity becomes nearly uniform along the filter channels, therefore promoting a quasi-uniform growth of the soot cake. Based on this meso-scale model, an additional numerical study from Bensaid et al. (14) demonstrated the influence of spatial soot deposit distribution on the filter regeneration process. They found that a fast regeneration of the filter promotes strong temperature gradients, where even small non-uniformities on the soot deposit distribution may be relevant for the evolution of the regeneration process.

Since a complete DPF is typically formed by thousands of channels, its numerical simulation with a standard meso-scale modeling approach similar to the one used by Bensaid et al. (14) would be computationally prohibitive, or at least would require the use of massive parallel computing. Nevertheless, as demonstrated by Konstandopoulos et al. (21), the fluid flow inside the narrow channels of DPF is nearly one-dimensional and the same applies for the local flow through the porous wall of the filter channels. Based on this perspective, macro-scale models (that may be also regarded as simplified meso-scale models) have been proposed and applied for modeling the soot filtration inside DPFs (20; 6; 22). Konstandopoulos et al. (6) extended the DPF model from Konstandopoulos and Johnson (20) for simulating high particulate loading effects. Their model assumes that the particulate loading is uniform along the filter channels and treats the flow inside these channels using a lumped approach, whereas the transient filtration at the filter wall is modeled using a one-dimensional approach by discretizing the wall into slabs of unit-collectors. This 1D model was validated against 3D CFD simulations of filtration inside a single filter channel, showing excellent agreement for the prediction of total pressure drop evolution with particulate loading. Recently, Konstandopoulos et al. (22) developed a model for supporting the design and optimization of asymmetric and variable cell geometry DPFs. Their model considers the 1D mass and momentum conservation laws for the flow along the filter channels as well as the 1D governing equations for the soot cake growth on the channels surface, where the

initial stage of filtration (depth filtration) inside the porous wall of the filter was neglected. Nevertheless, they adjusted the initial wall permeability in order to account for the influence of soot deposits formed during depth filtration. This modeling approach was found to yield predictions of pressure drop and cake thickness that are in good agreement with experimental data (excluding the initial stage of filtration) and hence, it can be employed for designing new filter configurations with lower pressure drop than the existing ones (23).

These models, based on different approaches, showed in the years acceptable and also truthful results. The majority of them were based on experimental validation showing their consistency compared to the experimental values (15; 24; 6; 22). In this respect, the present study is focused on the numerical modeling and simulation of soot filtration inside DPFs. The main objective is to propose a model that is developed based on already existing macro-scale models and is extended and improved in order to account for additional features, in particular being adapted to generic filter channel geometries. Furthermore, the proposed model is validated against available experimental results of soot filtration, where particular attention is given in identifying the main parametric uncertainties of the model (e.g. pressure drop across the filter). Due to the generic approach of the model, several DPF geometries are tested, obtaining, from the numerical point of view, some conclusions.

Filtration Model

The DPF model proposed here provides a meso-scale description of the flow along the inlet and outlet filter channels, which is coupled with a macro-scale description of the flow.

2.1 Fluid flow model at the filter channels scale

Let us consider a generic periodic element of DPF, as shown in Fig. 2.11 composed by inlet (1) and outlet (2) channels of length L, which are coupled by a porous wall (w) of thickness t_{w}. The flow along the filter channels is assumed to be one-dimensional in the axial direction z and, at every particular location in z, a fraction of the flow is allowed to cross the porous wall from the inlet to the outlet channel.
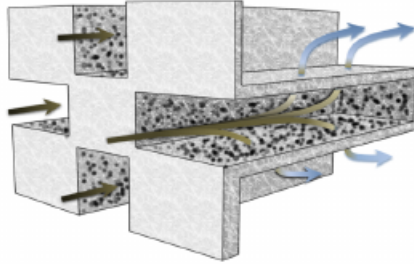
Figure 2.11: Generic DPF channels.

The cross-section areas $(A_1,\ A_2)$ and perimeters $(P_1,\ P_2)$ of the inlet and outlet channels, respectively, as well as the cross-section average perimeter at the wall P_{w} are kept generic in the sense that are not restricted to a particular filter channel geometry (e.g. square, triangular or hexagonal channels); although Fig. 2.11 shows the case of square channels, which is only one of the many geometries considered in the present study. For the clean filter, the cross-section area A_1 and perimeter P_1 of the inlet channel are denoted as A_{01} and P_{01}, respectively. During the filtration process, A_2, P_2 and $P_{\mathrm{w}} = (P_{01} + P_2)/2$ remain constant.

However, since a cake of thickness l_s grows on the top of the inlet surface of the porous wall, the cross-section geometry of the inlet channel is modified. Therefore, A_1 and P_1 are functions of the local l_s and can be expressed for a generic cross-section geometry as:

$$A_1(z) = A_{01} \left[1 - \frac{P_{01}}{2A_{01}} l_\mathrm{s}(z) \right]^2 \tag{2.1a}$$

$$P_1(z) = P_{01} \left[1 - \frac{P_{01}}{2A_{01}} l_\mathrm{s}(z) \right] \tag{2.1b}$$

due to the generic approach of the model, the equations 2.1 are also used to calculate A_1, A_2 at time $t = 0$ by substituting l_s with t_wall and f_1. In particular the model is able to provide different wall thicknesses to inlet and outlet channel thanks to f_1, fraction of wall to inlet channel as:

$$A_1 = A_{01} \left[1 - \frac{P_{01}}{2A_{01}} t_\mathrm{wall} f_1 \right]^2 \tag{2.2a}$$

$$P_1 = P_{01} \left[1 - \frac{P_{01}}{2A_{01}} t_\mathrm{wall} f_1 \right] \tag{2.2b}$$

$$A_2 = A_{02} \left[1 - \frac{P_{02}}{2A_{02}} t_\mathrm{wall} (1 - f_1) \right]^2 \tag{2.2c}$$

$$P_2 = P_{02} \left[1 - \frac{P_{02}}{2A_{02}} t_\mathrm{wall} / (1 - f_1) \right] \tag{2.2d}$$

Based on Fig. 2.11, the mass balances for the inlet and outlet filter channels are given as:

Inlet channel
$$\frac{d(A_1 \rho_1 v_1)}{dz} = -P_\mathrm{w} \rho_\mathrm{w} u_\mathrm{w} \tag{2.3a}$$

Outlet channel
$$\frac{d(A_2 \rho_2 v_2)}{dz} = P_\mathrm{w} \rho_\mathrm{w} u_\mathrm{w} \tag{2.3b}$$

where the axial gas velocities along the inlet and outlet channels (v_1 and v_2, respectively) are coupled to each other by the gas through-wall velocity u_w. Additionally, the momentum balances for the inlet and

outlet channels as well as for the porous wall of the filter are given as:

Inlet channel

$$A_1 \frac{dp_1}{dz} + \frac{d\left(A_1\rho_1 v_1^2\right)}{dz} = -f_1 P_1 \frac{1}{2}\rho_1 v_1^2 - P_{\mathrm{w}}\rho_{\mathrm{w}} u_{\mathrm{w}} v_1 \qquad (2.4\mathrm{a})$$

Outlet channel

$$A_2 \frac{dp_2}{dz} + \frac{d\left(A_2\rho_2 v_2^2\right)}{dz} = -f_2 P_2 \frac{1}{2}\rho_2 v_2^2 + P_{\mathrm{w}}\rho_{\mathrm{w}} u_{\mathrm{w}} v_2 \qquad (2.4\mathrm{b})$$

Porous wall

$$p_1 - p_2 = \mu_{\mathrm{w}} u_{\mathrm{w}} \left(\frac{l_{\mathrm{w}}}{K_{\mathrm{w}}} + \frac{l_{\mathrm{s}}}{K_{\mathrm{s}}} F_{\mathrm{c}}\right) \qquad (2.4\mathrm{c})$$

where the pressure distribution along the inlet and outlet channels (p_1 and p_2, respectively) determines the gas through-wall velocity distribution in the axial direction z.

The calculation of pressure drop along the inlet and outlet channels requires the evaluation of the Fanning friction factors f_1 and f_2 appearing in Eqs. (2.4a) and (2.4b), respectively, which are obtained as:

$$f_{\mathrm{j}} = \frac{c_{\mathrm{j}}}{\mathrm{Re}_{\mathrm{j}}} \qquad \mathrm{Re}_{\mathrm{j}} = \frac{\rho_{\mathrm{j}} v_{\mathrm{j}} D_{\mathrm{h,j}}}{\mu_{\mathrm{j}}} \qquad D_{\mathrm{h,j}} = \frac{4A_{\mathrm{j}}}{P_{\mathrm{j}}} \quad , \mathrm{j} = 1,2 \qquad (2.5)$$

where the Reynolds number Re for the channel flow is based on the respective hydraulic diameter D_{h} of the channel, and the friction parameter c depends on the channel cross-section geometry (25).

Since the total pressure drop of the filter is relatively small and the filtration process is isothermal, one assumes that the gas density is uniform inside the complete filter system (i.e. $\rho_1 = \rho_2 = \rho_{\mathrm{w}}$) and is calculated using the ideal gas law with specified reference pressure p_{ref} and temperature T_{ref}. Additionally, the same is assumed for the gas dynamic viscosity (i.e. $\mu_1 = \mu_2 = \mu_{\mathrm{w}}$) that is also calculated based on these reference conditions.

In a similar manner to A_1 and P_1, the correction factor $F_{\mathrm{c}} \in [1,\infty[$ appearing in Eq. (2.4c), which accounts for the variation of through-wall velocity along the cake layer, is also a function of the local soot cake thickness and is given for a generic cross-section geometry as:

$$F_{\mathrm{c}}(z) = -\frac{P_{\mathrm{w}}}{P_{01}} \left[\frac{P_{01}}{2A_{01}} l_{\mathrm{s}}(z)\right]^{-1} \ln\left[1 - \frac{P_{01}}{2A_{01}} l_{\mathrm{s}}(z)\right] \qquad (2.6)$$

Additionally, the average permeability of filter wall K_{w}, appearing in Eq. (2.4c), is not a constant but changes during the initial stage of

filtration (depth filtration) due to soot deposition inside the porous wall, and its calculation is explained in end of section 2.3.

The boundary conditions for Eqs. (2.3) and (2.4) are given according to Fig. 2.11 as:

$$z = 0 \ : \quad \begin{cases} v_1(0) = \dot{m}_{\mathrm{in}}/(A_1 \rho_1) \\ v_2(0) = 0 \end{cases} \tag{2.7a}$$

$$z = L \ : \quad \begin{cases} v_1(L) = 0 \\ p_2(L) = p_{\mathrm{out}} \end{cases} \tag{2.7b}$$

where $\dot{m}_{\mathrm{in}}$ is the mass flow rate of gas entering the inlet channel, which transports the soot particles to be filtered, and p_{out} is the pressure at the outlet of the filter.

The meso-scale simplified model described above is used for predicting the fluid flow at the scale of filter channels (i.e. v_1, v_2, p_1, p_2 and u_{w}) and it must be coupled with a filtration model at the porous wall scale in order to calculate the soot deposition and cake formation inside the filter, which dictates the time evolution of the geometric parameters and associated effective properties of the filter channels and porous wall (A_1, P_1, f_1, F_{c}, l_{s}, K_{w}).

2.2 Filtration model at the porous wall scale

For a particular location along the axial coordinate z of the filter channels, let us consider the one-dimensional filtration process where a gas flow transports poly-disperse particles of S different sizes through the porous filter wall, as sketched in Fig. 2.12.
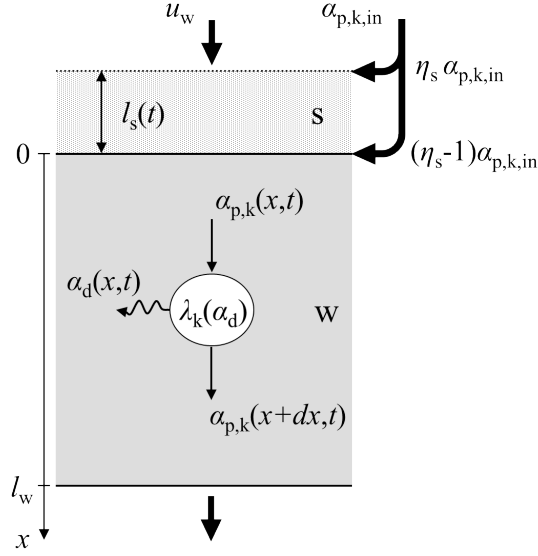
Figure 2.12: One-dimensional schematic representation of the depth filtration process.

Based on the homogenization approach, the volume fraction $\alpha_{p,k}$ of particles of size class k in the gas along the depth of porous wall is governed, at every instant, by a logarithmic law; see Eq. (2.8a). The total volume fraction α_p of all particles in the gas is calculated from Eq. (2.8b). Additionally, the time evolution of the local volume fraction α_d of particulate deposit inside the porous wall is governed by the local balance of particulate mass flow and deposition; see Eq. (2.8c).

$$\frac{\partial \alpha_{p,k}(x,t)}{\partial x} = -\lambda_k(\alpha_d)\,\alpha_{p,k}(x,t)\,,\ \forall_{k=1,\dots,S} \tag{2.8a}$$

$$\alpha_p(x,t) = \sum_{k=1}^{S} \alpha_{p,k}(x,t) \tag{2.8b}$$

$$\phi_d\,\frac{\partial \alpha_d(x,t)}{\partial t} = u_w \sum_{k=1}^{S} \lambda_k(\alpha_d)\,\alpha_{p,k}(x,t) \tag{2.8c}$$

where the packing solid fraction of deposit ϕ_d (i.e. the ratio of deposit density to particle density) is assumed to be constant in the present study. Nevertheless, for each particle size class k, the filtration coefficient λ_k is a function of α_d and hence, it depends on both time t and location x due to the continuous particulate deposition within the filter wall; see section 2.3.

Let us consider a clean filter wall with uniform properties at the beginning of the filtration process, which is totally free of particulate deposit. Additionally, let us assume a volume fraction $\alpha_{p,k,in}$ for each particle size

class k approaching the filter wall. Based on these considerations, the initial and boundary conditions for Eqs. (2.8) are given as:

$$t = 0 : \quad \alpha_{\mathrm{d}}(x, 0) = 0 \Rightarrow \lambda_{\mathrm{k}}(\alpha_{\mathrm{d}}) = \lambda_{\mathrm{k}}(0) \, , \, \forall_{x \in [0,L]} \tag{2.9a}$$

$$x = 0 : \quad \alpha_{\mathrm{p,k}}(0, t) = [1 - \eta_{\mathrm{s}}(t)] \, \alpha_{\mathrm{p,k,in}} \, , \, \forall_{\mathrm{k}=1,\ldots,S} \quad \forall_{t \geq 0} \tag{2.9b}$$

where the partition coefficient $\eta_{\mathrm{s}} \in [0, 1]$ is a controlling parameter, which determines the fraction of particles approaching the filter wall that contribute to cake formation on the top of the wall surface, as sketched in Fig. 2.12. The parameter η_{s} is given as a function of the volume fraction of particulate deposit at the filter wall inlet, i.e. $\alpha_{\mathrm{d}}(0, t)$, and its expression is discussed in section 2.3. The time evolution of the particulate cake thickness l_{s} is governed by the following mass balance and associated initial condition:

$$\phi_{\mathrm{s}} \frac{d \, l_{\mathrm{s}}(t)}{dt} = u_{\mathrm{w}} \, \eta_{\mathrm{s}}(t) \sum_{k=1}^{S} \alpha_{\mathrm{p,k,in}} \tag{2.10a}$$

$$t = 0 : \quad l_{\mathrm{s}}(0) = 0 \tag{2.10b}$$

where the packing solid fraction of cake ϕ_{s} (i.e. the ratio of cake density to particle density) is assumed to be constant.

2.3 Closure expressions for model parameters

Konstandopoulos et al. (6) originally proposed a function for the partition coefficient η_{s}, which was formulated based on the blocked-area fraction at the scale of unit-collector and implicitly depends on the volume fraction of particulate deposit at the filter wall inlet, i.e. on $\alpha_{\mathrm{d}}(0, t) \equiv \alpha_{\mathrm{d},0}(t)$. In the present study, the partition coefficient is generalized as some function of $\alpha_{\mathrm{d},0}$ and alternative expressions for $\eta_{\mathrm{s}}(\alpha_{\mathrm{d},0})$ are discussed in this section. Note that $\alpha_{\mathrm{d},0}$ must always lay in the range $[0, \varepsilon_0]$, where ε_0 is the initial porosity for the clean filter.

Independently of its form, η_{s} should always respects the following constrains: $\eta_{\mathrm{s}} = 0$ for a clean filter ($\alpha_{\mathrm{d},0} = 0$), and $\eta_{\mathrm{s}} = 1$ at the end of the depth filtration regime ($\alpha_{\mathrm{d},0} = \varepsilon_0$). In this respect, η_{s} defines the transition between depth filtration and cake formation regimes, where the critical time at which the depth filtration regime ends can be determined as the time when η_{s} becomes equal to 1, i.e. clogging occurs at the inlet of the porous wall. Under this condition, no more particles are

allowed to enter into the filter wall and hence, they will all contribute to the cake formation on the top of the filter wall surface (see Fig. 2.12).

If no detailed information is available about the transition between depth filtration and cake formation regimes, a simple expression for $\eta_s(\alpha_{d,0})$ can be formulated by assuming a step transition between these filtration regimes, which is given as:

$$\eta_s(\alpha_{d,0}) = \begin{cases} 0 \,, & \alpha_{d,0} < \varepsilon_0 \\ 1 \,, & \alpha_{d,0} = \varepsilon_0 \end{cases} \tag{2.11}$$

Alternatively, $\eta_s(\alpha_{d,0})$ can be formulated as a smooth transition function that apparently is more realistic since it allows the cake formation to start before the ending of the depth filtration regime (6). The present study proposes the following empirical function for the partition coefficient:

$$\eta_s(\alpha_{d,0}) = \left[1 + a^b \left(\left[\frac{\alpha_{d,0}}{\varepsilon_0} \right]^{-b} - 1 \right) \right]^{-1/b} \tag{2.12}$$

where $a \in [0,1]$ and $b \in]0, \infty[$ are adjustable parameters that define the transition process. It can be demonstrated that for $b \gg 1$, Eq. (2.12) converges to the original partition coefficient function proposed by Konstandopoulos et al. (6).

Based on the unit collector filtration theory, the filtration coefficient $\lambda_k(\alpha_d)$ for a particular particle size class k, required for solving Eqs. (2.8) and (2.9), is given as (6):

$$\lambda_k = \frac{\eta_{c,k}}{d_{por}} \tag{2.13}$$

where d_{por} and $\eta_{c,k}$ are the filter wall pore diameter and unit collector filtration efficiency for particle size class k, respectively, which implicitly depend on the particulate loading of the filter wall, i.e. on α_d. The pore diameter d_{por} is related to the filter wall porosity ε and unit-collector diameter d_c, and hence to α_d, as follows (6):

$$d_{por} = d_c \frac{2}{3} \frac{\varepsilon}{1 - \varepsilon} \tag{2.14a}$$

$$\varepsilon = \varepsilon_0 - \alpha_d \tag{2.14b}$$

$$d_c = d_{c,0} \left[\frac{1 - \varepsilon_0 + \alpha_d}{1 - \varepsilon_0} \right]^{1/3} \tag{2.14c}$$

where $d_{c,0}$ is the initial unit-collector diameter for the clean filter.

In order to determine $\eta_{c,k}$ based on the mechanisms of Brownian diffusion (D) and interception (R), the following closure expressions are required (6):

$$\eta_{c,k} = 1 - (1 - \eta_{D,k})(1 - \eta_{R,k}) \tag{2.15a}$$

$$\eta_{D,k} = 3.5\, g(\varepsilon)\, \mathrm{Pe}_k^{-2/3} \tag{2.15b}$$

$$\mathrm{Pe}_k = \frac{(u_w/\varepsilon)\, d_c}{D_{p,k}} \tag{2.15c}$$

$$\eta_{R,k} = 1.5\ g(\varepsilon)^3\ \frac{N_{R,k}{}^2}{[1 + N_{R,k}]^{(3-2\varepsilon)/(3\varepsilon)}} \tag{2.15d}$$

$$N_{R,k} = \frac{d_{p,k}}{d_c} \tag{2.15e}$$

$$g(\varepsilon) = \left[\frac{\varepsilon}{2 - \varepsilon - \frac{9}{5}(1-\varepsilon)^{1/3} - \frac{1}{5}(1-\varepsilon)^2} \right]^{1/3} \tag{2.15f}$$

$$D_{p,k} = \frac{k_B\, T_g}{3\, \pi\, \mu_g\, d_{p,k}}\, \mathrm{SCF} \tag{2.15g}$$

$$\mathrm{SCF} = 1 + \mathrm{Kn}\left(1.257 + 0.4\exp\left[-\frac{1.1}{\mathrm{Kn}} \right] \right) \tag{2.15h}$$

$$\mathrm{Kn} = \frac{2\, \ell_g}{d_{por}} \tag{2.15i}$$

where the symbols have their usual meaning according to (6) and the gas properties are obtained based on the reference conditions for pressure p_{ref} and temperature T_{ref}.

Although the unit-collector filtration model, given by Eqs. (2.13) to (2.15), provides a general approach for estimating λ_k for different filter wall morphologies, its simplicity is also associated to model uncertainties in defining the geometric parameters of the filter wall. Therefore, a more accurate approach for evaluating λ_k could be to perform micro-scale simulations of the filtration process taking into account the detailed morphology of the filter wall (17). Nevertheless, this alternative approach is computationally very expensive and is limited to the particular filter wall considered for the micro-scale simulations.

The average permeability of filter wall K_w, required by Eq. (2.4c) at a particular location along the axial coordinate z, is calculated at every instant from the respective local permeability K_w along the wall depth

using the following relation based on serial arrangement:

$$\frac{L}{K_{\mathrm{w}}} = \int_0^L \frac{1}{K_{\mathrm{w}}(x)} \, dx \qquad (2.16)$$

where K_{w} is estimated by (14; 26):

$$K_{\mathrm{w}}(x) = K_0 \frac{1 - \varepsilon_0}{1 - \varepsilon} \frac{\left[2 - \varepsilon - \frac{9}{5}(1 - \varepsilon)^{1/3} - \frac{1}{5}(1 - \varepsilon)^2\right]}{\left[2 - \varepsilon_0 - \frac{9}{5}(1 - \varepsilon_0)^{1/3} - \frac{1}{5}(1 - \varepsilon_0)^2\right]} \left(\frac{d_{\mathrm{c}}}{d_{\mathrm{c},0}}\right)^2 \mathrm{SCF}$$
$$+ K_{\mathrm{s}} \, \alpha_{\mathrm{d}} \qquad (2.17)$$

based on the permeability K_0, porosity ε_0 and collector diameter $d_{\mathrm{c},0}$ of the clean filter wall. Additionally, ε, d_{c} and SCF are calculated using Eqs. (2.14b), (2.14c) and (2.15h), respectively, which are functions of the local α_{d} predicted from the solution of Eqs. (2.8) and (2.9). Note that the last term in Eq. (2.17) is included in order to prevent K_{w} from going to zero if $\alpha_{\mathrm{d}} \to \varepsilon_0$ due to local clogging of the filter wall.

2.4 Model testing conditions

Since the structure of the DPFs is basically a honeycomb, with all the corresponding characteristics (e.g. constant size, parallel channels), the geometries are obtained by repeating a constant periodic element. In this work, several geometries are studied referring to the periodic element of each geometry.

All the simulations are carried out referring to certain specific conditions. In order to get a comparison from the geometries investigated, two exhaust gas conditions are tested along the present work. Due to the complexity of the simulation parameters, the exact conditions of the flow are realistic and justified in terms of literature references.

In Table 2.1, the first testing conditions are shown. These conditions are similar to the ones used by Murtagh et al. (7) (then used by Kostandopoulos et al. (6)). They represent well-known and consistent conditions, since used not only in the previous works but also by Lupše et al. (15) for similar scopes.

The loading conditions presented in Table 2.1, depict an average exhaust flow rate approaching the DPF, these conditions could represent an exhaust flow rate of a heavy duty engine. Some of the parameters in Table 2.1 are not exactly the same used by Kostandopoulos et al. (6), in

	Parameter	Value	Reference
External Conditions	v_{appr} (m/s)	7.56	(6)
	P (Pa)	1.0×10^5	(6)
Filter characteristic	l (m)	0.3048	(6)
	t_{wall} (m)	431.8×10^{-6}	(6)
Exhaust gas conditions	p_{gas} (Pa)	1.0×10^5	(6)
	T_{gas} (K)	533.0	(6)
	M_{gas} (kg/mol)	28.97×10^{-3}	(6)
	μ_{gas} $(Pa \times s)$	2.64×10^{-5}	(6)
Cake parameters	ρ_s (kg/m^3)	80.0	
	K_s (m^2)	2.2×10^{-14}	(6)
Deposit parameters	ρ_d (kg/m^3)	5.0	
Particles condition	d_{part} (m)	180.0×10^{-9}	(6)

Table 2.1: Testing conditions #1.

Table 2.2 are shown the values compared with the values of the reference. The deviation is introduced due to experience on the field and comparison with the literature (experimental results obtained by Koltsakis et al. (27)).

Parameter	Simulation Value	Reference Value
Cake density ρ_s kg/m^3	80.0	91.0
Deposit density ρ_d kg/m^3	5.0	8.26

Table 2.2: Differences between the values used to perform the simulation and the reference of Kostandopoulos et al. (6).

A second set of conditions is used to test the model, shown in Table 2.3. The conditions are intended to be referred to different slower loading conditions. These conditions are mainly in concordance with the experimental investigation of Bensaid et al. (8). One could see that the deviations regard only few parameters of the gas conditions, in fact, the other conditions (e.g. geometric conditions of the filter...), are in concordance with the ones in Table 2.1.

	Parameter	Value	Reference
External Conditions	v_{appr} (m/s)	1.84	(8)
	P (Pa)	1.0×10^5	(6)
Filter characteristic	l (m)	0.3048	(6)
	t_{wall} (m)	431.8×10^{-6}	(6)
Exhaust gas conditions	p_{gas} (Pa)	1.0×10^5	(6)
	T_{gas} (K)	533.0	(6)
	M_{gas} (kg/mol)	28.97×10^{-3}	(6)
	μ_{gas} $(Pa \times s)$	2.64×10^{-5}	(6)
Cake parameters	ρ_s (kg/m^3)	25.0	(8)
	K_s (m^2)	1.1×10^{-14}	(8)
Deposit parameters	ρ_d (kg/m^3)	2.5	(8)
Particles condition	d_{part} (m)	180.0×10^{-9}	(6)

Table 2.3: Testing conditions #2.

The approach to the code leads it to be as general as possible. The geometries are investigated, in fact, having a symmetric and an asymmetric filter wall distribution. The way to obtain the asymmetric distribution is clarified along the present work.

Some dimensionless parameters are introduced to allow parametric studies. The first parameter is r_{120} which represents the ratio of inlet channel area to outlet channel area (neglecting filter wall), showed in Equation 2.18a. The other parameter is r_{wp0}, which is the ratio of the inlet perimeter to the square root of element area, shown in Equation 2.18b.

$$r_{120} = \frac{A_{10}}{A_{20}} \tag{2.18a}$$

$$r_{\text{wp}} = \frac{P_i}{\sqrt{A_e}} \tag{2.18b}$$

2.5 Geometries: method and design

The present work analyzes some geometries, it also includes a specific wall thickness distribution changing method. In fact, some geometries are obtained from the ones but including a different wall thickness distribution. Starting from symmetric geometries, by keeping constant the wall thickness, several asymmetric geometries are created. The central hypothesis of the work is to keep constant the wall thickness. This hypothesis guarantees a qualitative constant mechanical resistance of the filter, in fact the thickness wall is usually an important parameter dealing with the mechanical resistance and the manufacturing limits.

The literature is giving attention to the design of the cell and many works are facing this aspect (22; 6; 28; 29). The most common geometry on the market has an equal square shape for the inlet and the outlet channels. For example, Corning mostly uses this design (12). The square shape with equal distribution of thickness to inlet and outlet is called in this work SQR-05. This geometry is well-known in the literature and used for either experimental and numerical analysis ((8; 14; 6; 15; 28)), this is one of the reasons why it is included in the present study. It is recognized as the conventional DPF design. This case is also used in the present paper for the validation of the model (see section 3.2).

The name (SQR-05) underlines the importance of the parameter f_1, defined in the Equation 2.19.

$$f_1 = \frac{wall - fraction_{(inlet)}}{wall - fraction_{(outlet)}} \qquad (2.19)$$

A different distribution of the wall thickness affects the open frontal area of the filter. We will see along the work as this parameter could have advantages/disadvantages depending on how the geometry changes.

Figure 2.13 shows the square/square geometry with equal distribution of the filter wall to the outlet/inlet channels.
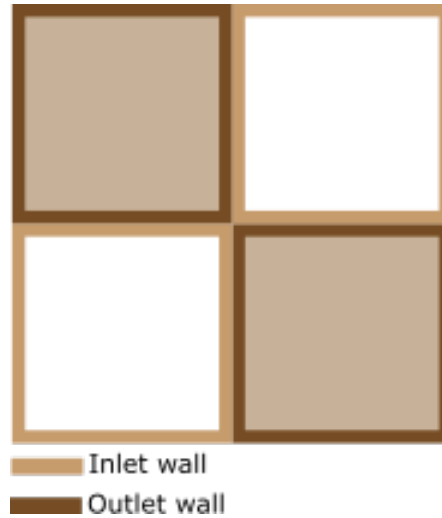
Figure 2.13: SQR geometry: $f_1 = 0.5$.

Different colors are used in order to identify and distinguish inlet and outlet thickness wall. It has to be underlined that the different walls are here denoted with different colors, in reality, they are manufactured

with the same process. Colors white and grey respectively depict inlet channels and outlet channels.

Figure 2.14-2.15-2.16-2.17 clearly illustrate the wall thickness distribution strategy. To facilitate the wall thickness growing side, some arrows are included. Starting from SQR-05 geometry other geometries are obtained. Different colors are used for different wall and different channels to better identify the differences.
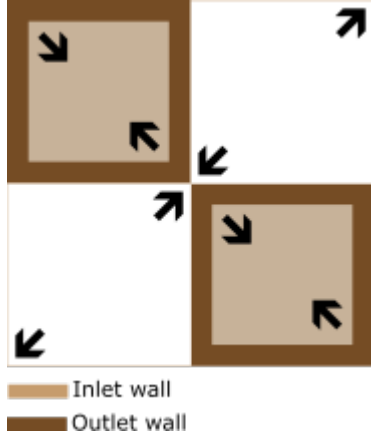
Figure 2.14: SQR geometry: $f_1 = 0.0$.

Figure 2.15: SQR geometry: $f_1 = 0.25$.

Figure 2.16: SQR geometry: $f_1 = 0.75$.

Figure 2.17: SQR geometry: $f_1 = 1.0$.

In this way the following geometries are introduced:

- $f_1 = 0.0$: Entire wall thickness to the outlet channel. The inlet channel is maximized (Figure 2.14). Called in this work: SQR-00;

- $f_1 = 0.25$: Partial wall thickness to inlet and outlet channel (Figure 2.15). Called in this work: SQR-025;

- $f_1 = 0.5$: Symmetric distribution of the wall thickness to inlet and outlet channel (Figure 2.13). Called in this work: SQR-05;
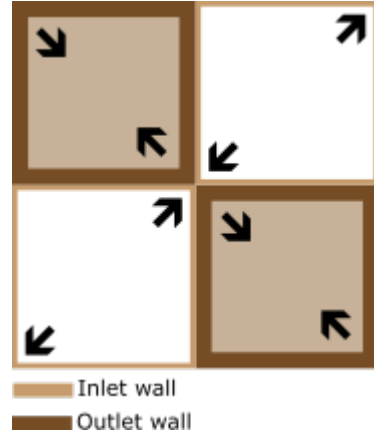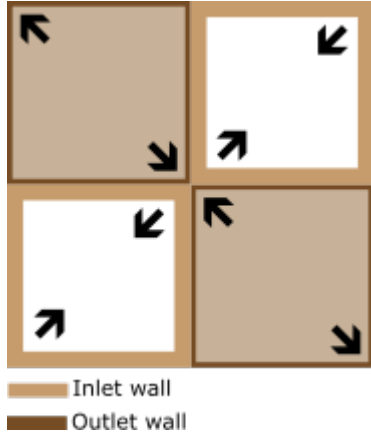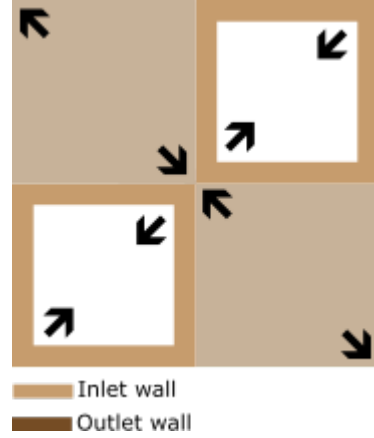
- $f_1 = 0.75$: Partial wall thickness to inlet and outlet channel (Figure 2.16). Called in this work: SQR-075;

- $f_1 = 1.0$: Entire wall thickness to the inlet channel. The outlet channel ares is maximized (Figure 2.17). Called in this work: SQR-10;

The detailed description of the new geometries obtained due to the wall thickness distribution strategy is clearly explained above. The same approach is used for the other geometries. As seen above, it is also described the abbreviations of the geometries introduced, this naming procedure is used for the other geometries in the same way.

The previous images represent the periodic element of the filter. It has to be noted that the filter is a repetition of equal cells. In the present work, the geometric changes are obtained starting from the periodic element area of the filter. This is the familiar approach used in the literature as well.

Obtaining the total filter shape is the consequent repetition of several periodic element areas. For each geometry, the total shape of the filter is showed. Figure 2.18 shows the structure and the aspect of the filter.
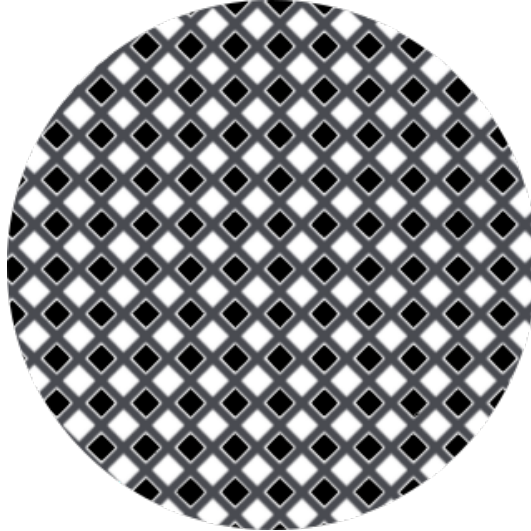
Figure 2.18: SQR-05 geometry: filter structure.

The different colors (black and white) represent, respectively, the plugged and unplugged channels of the filter. Thep point of view of Figure 2.18 could represent the perspective that the exhaust gases face

coming from the exhaust manifold.

Another geometry here presented, is composed of two equal triangular channels. This shape is widely investigated by Konstandopoulos et al. (30). Figure 2.19 shows the structure of the periodic element of the geometry. Different colors have been included in order to identify wall portion to inlet/outlet channels. Specifically, Figure 2.19 shows the periodic element area of TRI-05 with a fraction f_1 equal to 0.5.
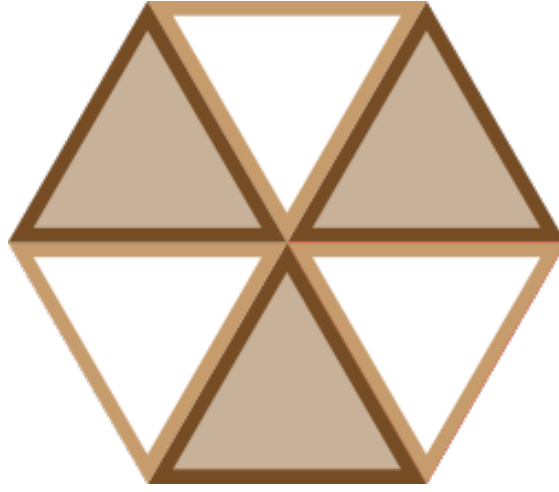
Figure 2.19: TRI-05 geometry: elementary structure.

Figure 2.20 shows the aspect of the filter structure. It displays plugged and unplugged channels, they represent inlet/outlet channels of the filter.
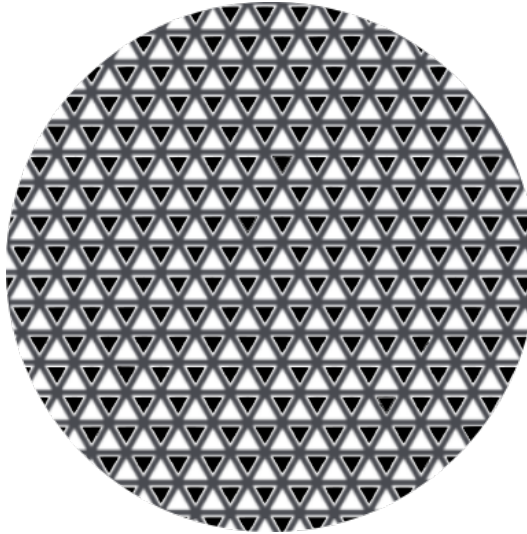
Figure 2.20: TRI-05 geometry: filter structure.

Starting from TRI-05, as well as for SQR-05, other geometries are

obtained thanks to an asymmetric distribution of the filter wall to the inlet/outlet channels. The distinctions in terms of geometry nomenclature and fraction f_1 are here summarized:

- TRI-00, $f_1 = 0.0$;

- TRI-025, $f_1 = 0.25$;

- TRI-05, $f_1 = 0.5$;

- TRI-075, $f_1 = 0.75$;

- TRI-10, $f_1 = 1.0$.

The logic of the process is the same already seen above for SQR-XY geometry. By keeping constant the wall thickness, several geometries are obtained due to a different distribution of the filter wall to inlet and outlet channels.

The asymmetric geometries are investigated in literature in order to provide a better design for diesel particulate filters. The trend is to develop different designs with a greater surface area for the cake to grow up and a greater inlet channel area, more open compared to conventional design. For this reason, a hexagon-triangular geometry has been introduced and studied for some years. In the literature Majewsky et al. (5) analyzed some asymmetric geometries including this one. Apparently, this geometry shows the changes desired to improve the conventional geometries performances:

- it has a greater inlet area. Outlet channels are smaller than the inlet channel area;

- the surface available for the cake to grew up is bigger. Hexagon shape guarantees a good ratio perimeter\area.

In reality, this geometry gives good results only in certain conditions, it will be investigated along the present work. Figure 2.21 shows the periodic element of the geometry under investigation. As previously indicated in Figures 2.19-2.13, it is illustrated the distinction between thickness wall to inlet/outlet channels.
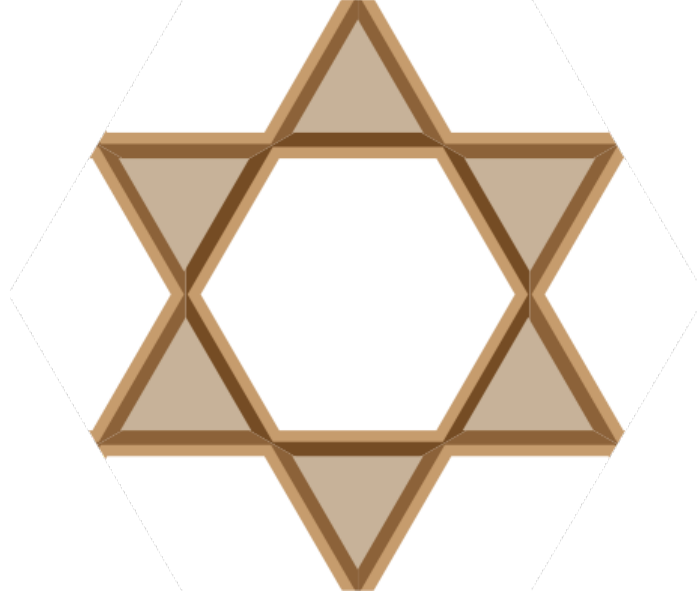
Figure 2.21: HEX-TRI-05 geometry: elementary structure.

Figure 2.22 shows the filter structure of HEX-TRI-05 design. It is possible to identify the inlet and outlet channels. As described above, it follows the trend to provide a greater surface area for storing the ash, leaving the ash-filled inlet channels more open than the conventional design. Figure 2.22 shows the inlet channels (unplugged) in white, the wall in grey while the outlet channels (plugged) are in black.
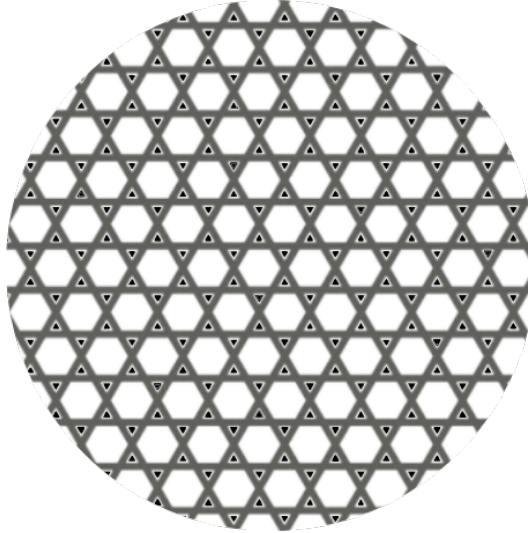
Figure 2.22: HEX-TRI-05 geometry: filter structure.

Another geometry introduced during the technological development of the diesel particulate filter design is composed by an octagon inlet channel shape and a square outlet channel shape. It was commercialized in 2004 by Ibiden, for diesel passenger cars (Peugeot) (5). This design

is in concordance with the trend concerning the inlet channel area and the area available to develop the cake inside the inlet channels.

In this work, octagon-square geometry is called OCT-XY, where XY indicates the decimal part of f_1. Figure 2.23 shows the elementary structure of the geometry with $f_1 = 0.5$, which represents the symmetric wall thickness distribution. Different colors are used for inlet/outlet channels and for inlet/outlet wall thicknesses.
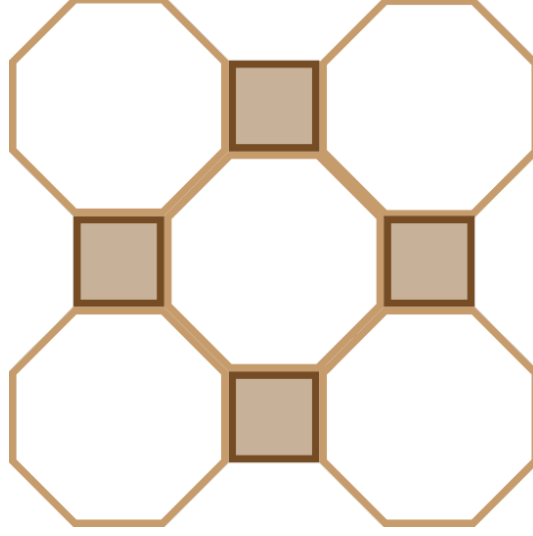
Figure 2.23: OCT-05 geometry: elementary structure

Figure 2.24 shows the filter structure for the octagon-square geometry with an equal distribution of wall thickness to the inlet and outlet side. Starting from the symmetric distribution of the wall (case: $f_1 = 0.5$) other geometries with asymmetric distribution of the wall thickness are obtained. It leads to following geometries:

- OCT-00, $f_1 = 0.0$;

- OCT-025, $f_1 = 0.25$;

- OCT-05, $f_1 = 0.5$;

- OCT-075, $f_1 = 0.75$;

- OCT-10, $f_1 = 1.0$.
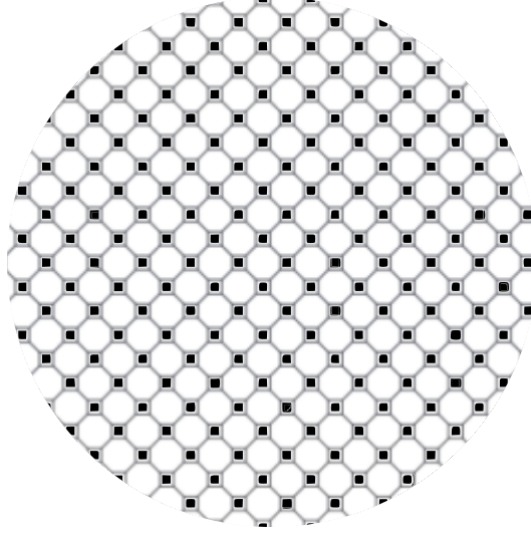
Figure 2.24: OCT-05 geometry: filter structure..

Another important geometry is designed with a hexagon shape to the inlet and outlet side. This geometry has been tested many times in literature, giving some important results. As for the previous geometries, Figure 2.25 shows the periodic element for the case: $f_1 = 0.5$. Other geometries are obtained from this case, by changing the wall thickness distribution to inlet/outlet channel. These cases are the same ones already explained for the other geometries (see wall thickness distribution for the previous geometries).
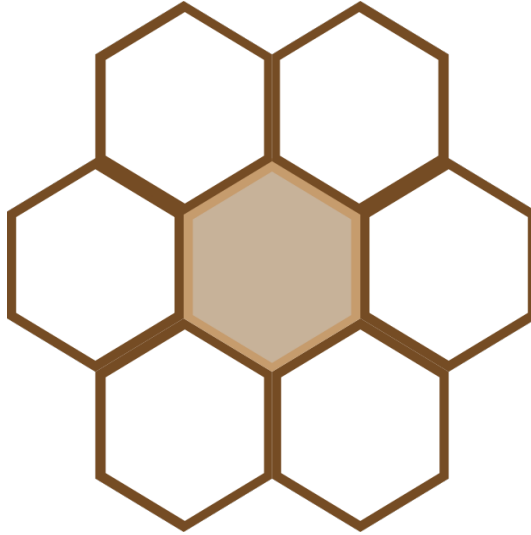
Figure 2.25: HEX-05 geometry: elementary structure

Figure 2.26 shows the corresponding filter structure of the elementary element showed in Figure 2.25. Different colors are used to underline the differences among the inlet channels, outlet channels and wall thicknesses.
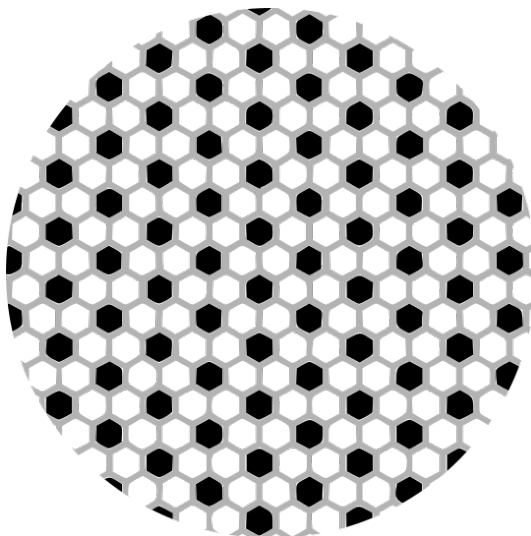
Figure 2.26: HEX-05 geometry: filter structure..

Results and Discussion

3.1   Resolution robustness of the model

Grid sensitivity and robustness tests are conducted in order to guarantee and analyze the stability of the results. The test concerns the resolution of the model along the inlet/outlet channels and the filter wall. Several 1D resolutions are tested getting some conclusions about the model stability. As indicated in Figure 3.27, DPF filters could be analyzed by dividing the study perimeter into several 1D paths. This is the typical way used to analyze DPF with 1D approaches (6; 31).
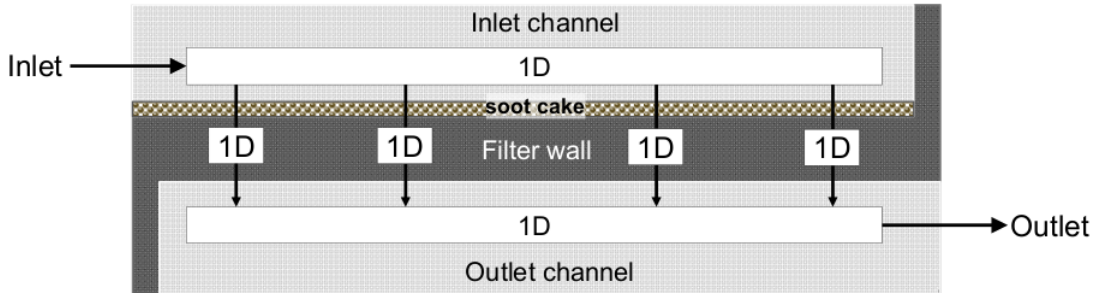
Figure 3.27: Filter model: process directions.

Two types of checks are done. As in Figure 3.27, both the channel direction and the wall direction are investigated. This highlights some important results about the grid independence of the model. The validations are carried out for two different geometries: SQR-05 and TRI-05.

In Figures 3.28-3.29 the results for the filter channel directions are shown. The results are illustrated in terms of time to get 250 *mbar* and periodic element area. The y-axis represents a maximum limit used to test and verify the robustness test over a large pressure drop range. The x-axis represents the DPFs channel densities. Four resolutions are investigated:

- 1 point,

34

- 10 points,

- 50 points,

- 100 points.

The results of the analysis are summed in Table 3.4, it shows the maximum difference compared to the 100 points resolution. From Figure 3.28-3.29 it is clear that after a certain resolution the model gives stable and constant values. Specifically after 10 points the model gives stable results.
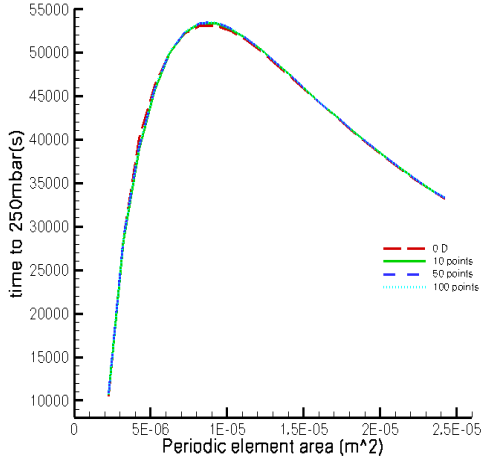
Figure 3.28: SQR-05 comparison.   Figure 3.29: TRI-05 comparison.
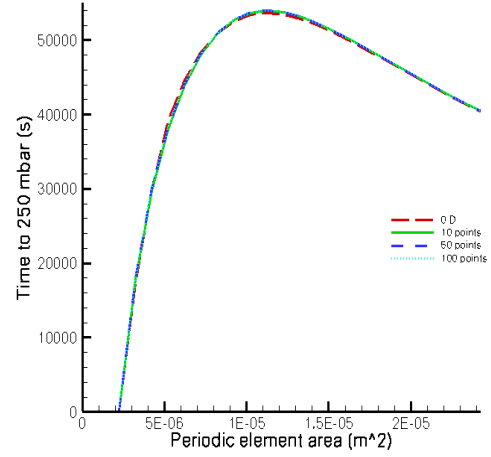
By looking at the differences among **the resolutions**, summed in Table 3.4, **a value of 20 points** can be stated as an optimal compromise between analysis time and stable results.

Grid resolution	Maximum difference with 100 points	
	SQR-05	TRI-05
1 point	2.51%	4.84%
10 points	1.40%	1.67%
50 points	0.31%	0.33%

Table 3.4: Resolution differences.

Besides the test for the resolution along the channels, another resolution check was done regarding the resolution through the filter wall (see Figure 3.27). As illustrated in Figure 3.30, the through-wall resolution is mainly modeled in two ways: a uniform and a non-uniform grid. As explained by Konstandopoulos et al. in (16), due to the "incoherent" distribution of the soot accumulation in the filter wall during the deep

bed filtration, a not uniform grid resolution through the filter wall, could represent a consistent approach. The not-uniform way is typically built up by having more grid point at the beginning of the wall (closer to the inlet side) than at the end of the wall. Anyway, the present model uses a uniform grid approach, which is another rational way to develop the model.
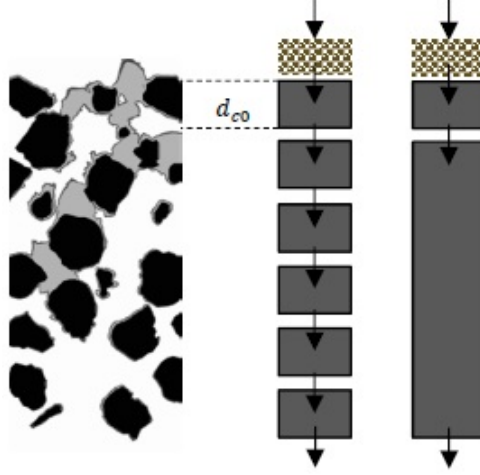
Figure 3.30: Filter model through the wall: a set of solutions.

In Figures 3.31-3.32, the results for the through-wall test are shown. The differences are bigger than the results obtained for the through channel test and the grid independence shows some limits in terms of grid resolution. In fact, by looking at the results sum in Table 3.5, comparing it with Table 3.4, the grid has to set over a certain grid resolution. For 5 or 10 points the simulations give incoherent results. A good compromise between analysis time and stable results could be using **a resolution of 50 points along the filter wall**.
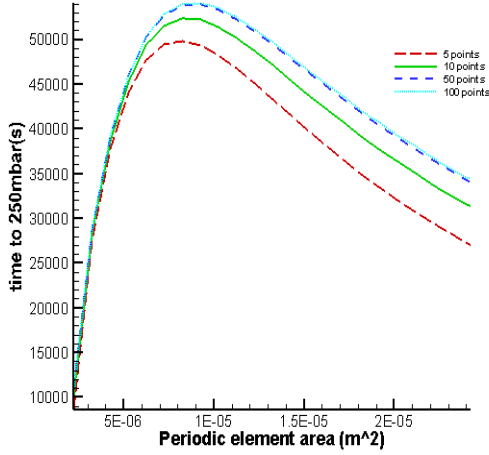
Figure 3.31: SQR-05: filter wall
resolution results.
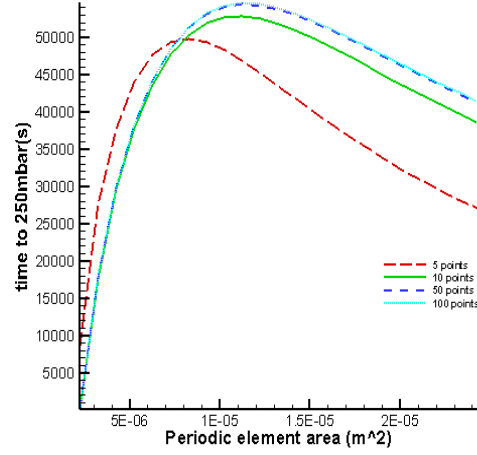
Figure 3.32: TRI-05: filter wall
resolution results.

	Maximum difference with 100 points	
Grid resolution	SQR-05	TRI-05
5 point	19.97%	17.34%
10 points	8.74%	7.08%
50 points	0.79%	0.65%

Table 3.5: Resolution differences.

3.2   Model validation

The validation of the model is obtained thanks to several experimental
data. The first reference uses data from Murtagh et al. (7). The same
comparison was also done by Konstandopoulos et al. (6) and Lupse et al.
(15). Konstandopoulos et al. used the data to fit and validate their 0D
model while Lupse et al, to validate a 1D model, that is in concordance
with the present work.

In Table 3.6 are showed the simulation parameters of the two filter tested
for the validation, Ex-47 and Ex-54 (both SQR-05 geometry). Either
d_{pore} and ϵ are given by the filter producer. Values of K_0 are typical for
the operation conditions (6) while values of $\rho_{soot,c}$ are obtained thanks
to the experience in the field for that testing condition.

According to the experimental conditions explained by Murtagh et al.
(7), the filters were exposed to the particulate mass flow of 18 gr/hr, this
value is assumed as the exact composition of solid particulate passing
through the filters (6). DPF's dimensions are 10.5"x12.0", with a cell

density of 100 cpsi and a wall thickness of 0.017 in. The filters are intended to be exposed to an exhaust flow rate of a heavy-duty engine, considering a flow rate of $0.236 Nm^3/s$ at $260°C$. More information are provided in the authentic paper (7) or in the other papers where this data are used (6; 15).

	EX-47	EX-54	Reference
$d_{pore}(\mu m)$	13.4	24.4	(6)
ϵ (%)	48	50	(6)
$K_0(m^2 \times 10^{-13})$	2.0	3.3	(15)
$\rho_{soot,c}(kg/m^3)$	69.0	68.0	

Table 3.6: Validation #1 and #2: parameters.
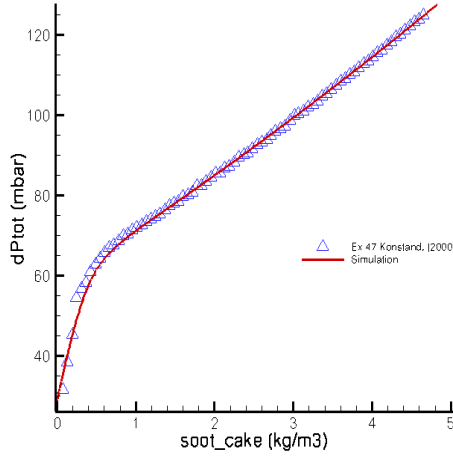
Figure 3.33: Comparison of pressure drop prediction of the code against the experiment (7) as reported in (6): curve provides for a Corning EX-47 filter.
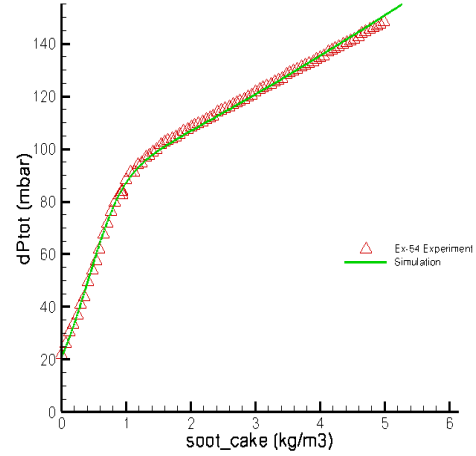
Figure 3.34: Comparison of pressure drop prediction of the code against the experiment (7) as reported in (6): curve provides for a Corning EX-54 filter.

Examining Figures 3.33 and 3.34 it is possible to observe as the simulations advance exactly like the two experiments, they recall exactly the experiments curves in the first and in the second transition (from deep bed filtration to cake formation evolution). The consistency of the model is confirmed for both cases.

In addition to the previous test, another one is provided in order to further confirm and guarantee the strength of the model even in different conditions. This case is referred to an experimental investigation of

Bensaid et al. (8). The original paper provides two different experiments with different filter housings, the present work is in accordance with the second methodology used in (8). The experimental apparatus consisted of a DPF filter (length 17.7 cm, diameter 2.54 cm) according to the geometrical parameters shown in Table 3.7 with a square cross-section geometry (SQR-05). The filter loading was obtained using a synthetic soot generator, consisting of a soot mass flow rate of 5 mg/h. The values of the first three lines of Table 3.7, are obtained thanks to the indications of Bensaid et al. (8), the last three lines of the same table are reached thanks to experience on the field. By comparing value of $\rho_{soot,c}$ with Table 3.6, it is clear the difference between the values. The main reason is the really different loading condition, which leads to a completely different approaching velocity to the filter, and a completely different deposition process. For the other parameters, the reader is referred to check the original paper (8).

	Value	Reference
$d_{pore}(\mu m)$	12.0	(8)
ϵ (%)	43	(8)
$CPSI(in^{-2})$	300	(8)
$K_0(m^2 \times 10^{-13})$	3.0	
$\rho_{soot,c}(kg/m^3)$	22.0	

Table 3.7: Validation #3: parameters.

The result of the validation test (Figure 3.35) shows as the model works recalling the experimental curve. As well as in the deep bed filtration transition and in cake formation transition, the model works well. This case is shown in terms of pressure drop inlet/outlet ($mbar$) compared to time (hours), different from the previous validation (Figure 3.33-3.34) where it is used soot cake (kg/m^3) in filter as x-axis variable.
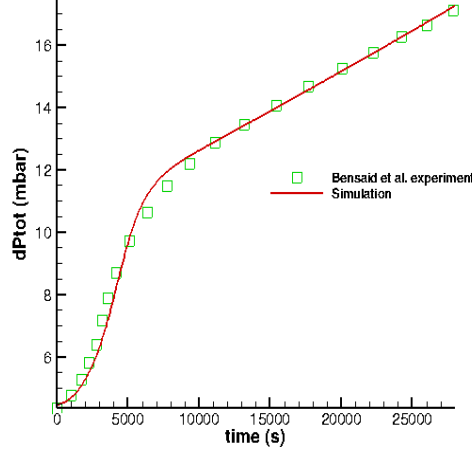
Figure 3.35: Comparison of pressure drop prediction of the code against the experiment shown in (8).

The result of the test (Figure 3.35) affirms the consistency of the model. It recalls, with good accuracy, the experimental points.

Due to this check, it is possible to underline the consistency of the model since three different cases are analyzed. This conclusion is confirmed thanks to the different experimental conditions taken into account.

3.3 Results

3.3.1 Overview for different wall thickness distribution

In this section, the results of the simulations are provided. Simulations parameters have been already analyzed and showed in Section 2.4. Basing on the wall thickness strategy, from some geometries many others are obtained. In Section 2.5 this method is clearly described. To sum up, here it is itemized the list of combinations;

- XY-00: $f_1 = 0.0$.

- XY-025: $f_1 = 0.25$.

- XY-05: $f_1 = 0.5$.

- XY-075: $f_1 = 0.75$.

- XY-10: $f_1 = 1.0$.

The periodic element area of the investigated geometries, is always composed of regular figures. This allows a correspondence among the

adjacent borders of periodic element areas. This is the reason why, by controlling few parameters of the periodic element area, it is possible to re-size it, keeping constant the ratio and the proportionality of the geometry. This method is widely investigated in literature as well, it is used to change the area of the periodic element. In order to obtain several filter densities, this parameter is changed. It has to be noted as, according to parameters reported in Section 2.5, all the geometries and filter densities simulations, are carried out with the same filter dimensions. By keeping constant the filter dimensions (length, width and height), the periodic element area is changed in order to obtain different filter density. Changing the periodic element area means re-sizing both the inlet and the outlet channels with the same proportion, in fact, the unique way to obtain an asymmetry in the filter structure, is the wall thickness distribution. Wall thickness distribution is mainly controlled by the parameter f_1.

Starting from the simulation conditions, a first important response comes from the reaction of the investigated geometries to different wall thickness distribution under the same testing conditions. This test is done for both the first and the second simulation conditions. In these tests, a specific periodic element area is chosen, while the fraction of wall to inlet/outlet channels is investigated. The limit condition for the simulations is set up to be the maximum pressure drop between intake and exhaust of the filter; this parameter is 150 *mbar*. Lifetime is this work, has to intended being time to reach a maximum pressure. Sometimes this lifetime is equivalent to the time of the clean filter to reach the first regeneration, it depends on the strategy used by the vehicle control unit. But often, the accumulated soot in the filter is calculated according to the pressure drop, that can be measured or predicted. Lifetime has to be accepted as a lifetime to regeneration and not a real lifetime of the filter that depends on many other parameters and, of course, it does not occur at the first regeneration (at least in the majority of the cases). Figures 3.36-3.37 show the results of the two tests. As admitted before, periodic element area is constant for both cases: $A_e = 9.25 \times 10^{-6}$ m. This is an indicative value, it could be chosen another one. For testing conditions #1 and #2 two different trends are obtained.
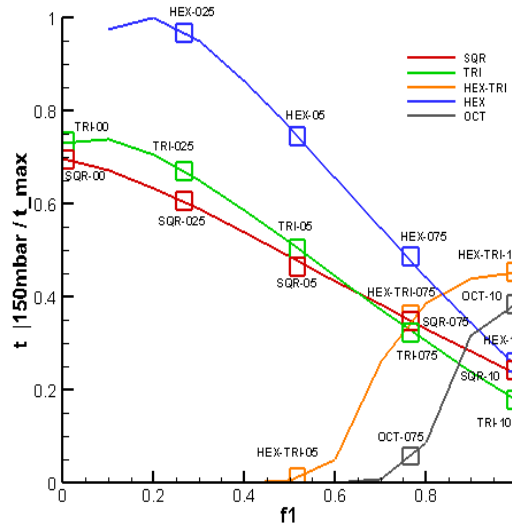
Figure 3.36: Different normalized lifetimes of several geometries by changing the wall thickness distribution. Periodic element area $= 9.25 \times 10^{-6}$. Test conditions # 1.
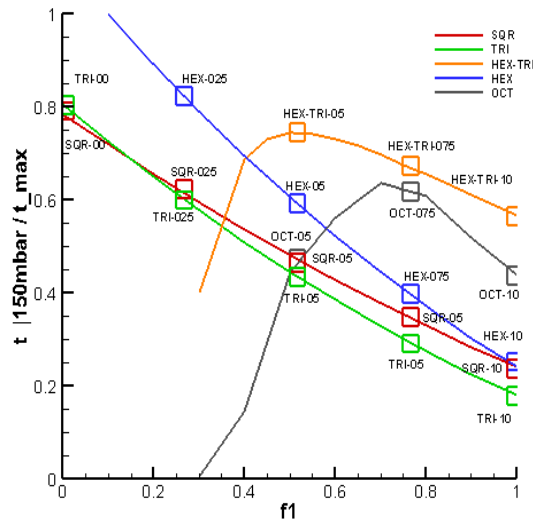
Figure 3.37: Different normalized lifetimes of several geometries by changing the wall thickness distribution. Periodic element area $= 9.25 \times 10^{-6}$. Test conditions # 2.

- For testing condition #1: Trends of the geometries change by giving different wall thickness distribution to inlet/outlet channels. SQR, TRI and HEX geometries increase the lifetime by decreasing the fraction of wall to the inlet side (bigger outlet channels). OCT and HEX-TRI geometries show an opposite trend. By increasing the

42

fraction of wall to inlet side (smaller inlet channel area), lifetime increases. This second conclusion has to be seen by checking the design criteria of the geometries showed in Section 2.5. In fact, OCT and HEX-TRI geometries have a bigger r_{120} ratio. It means that by decreasing f_1, the outlet channels area decreases too much and the velocity field in the outlet channels increases too much as well. This lead to an unfavorable increase of the pressure drop. Differently from this phenomena, by increasing f_1, the outlet channel area increases and the velocity field decreases, ending up with a lower pressure drop. This increases the lifetime of the filter;

- For testing condition #2: Trends of the geometries is similar to the one already seen for testing condition #1. SQR, TRI and HEX geometries increase the lifetime by decreasing the fraction of wall to the inlet side (bigger outlet channels). OCT and HEX-TRI geometries show an opposite trend. By increasing the fraction of wall to the inlet side (smaller inlet channel area), lifetime increases. Differently from the first case, here OCT and HEX-TRI geometries show different outputs, for $f_1 = 0.5$, the results are comparable with the other ones. HEX-TRI-05 lifetime is bigger than HEX-05, SQR-05 and TRI-05. OCT and HEX-TRI show a specific range where there is a maximum. HEX, SQR and TRI show a quasi-linear trend.

In Figures 3.36-3.37 there is an interruption in the HEX curve. By looking at the design of HEX geometry (see Section 2.5), a filter wall distribution with $f_1 = 0.0$, leads to a limit case. In fact, this would mean no filter wall to inlet side. The new geometry would be composed of only outlet channels (with a small area) immersed in an inlet channel with no perimeter. This cases, not only ideally but also physically, provide not comparable results with the "regular" geometries. Furthermore, it has to be noted that from the manufacturing point of view, it seems to be really difficult to realize such a specific geometry. In Figure 3.38 periodic element area of HEX-00 is indicated. The white zone, where the outlet channels are immersed represents the inlet channel area. There is no inlet channels wall thickness ($f_1 = 0.0$). Grey and brown represent the outlet channels and the filter wall to the outlet channels. The structure of the filter is indicated in Figure 3.39.
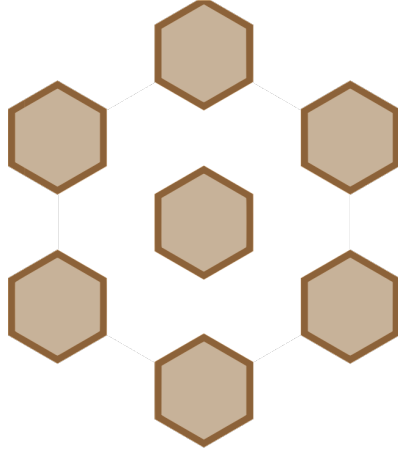
Figure 3.38: HEX-00 geometry: elementary structure.
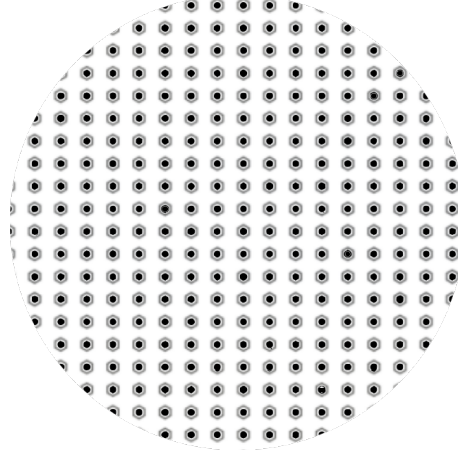
Figure 3.39: HEX-00 geometry: filter structure.

A similar trend to HEX-00 geometry, it appears for OCT-00 as well. Even if it is not shown in Figures 3.36-3.37, since for the velocity investigated this geometry shows inconsistent results, in case of $f_1 = 0.0$, OCT-00 would depict a limit case. In fact, by excluding the wall thickness to the outlet, inlet channels would lose the perimeter and only outlet channels would be part of the filter with a regular perimeter. This kind of design is not consistent with the physic of the phenomena. OCT geometry already has a big r_{120}, by reducing f_1 it would come out with a worse situation. As for HEX-00, OCT-00 was examined as well, the results are not comparable with the other ones. Figures 3.40-3.41 show the geometry here analyzed.
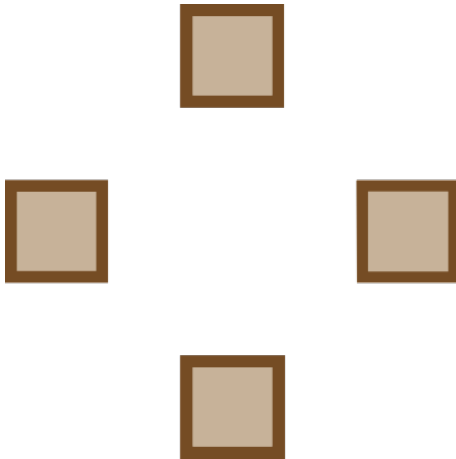
Figure 3.40: OCT-00 geometry: elementary structure.
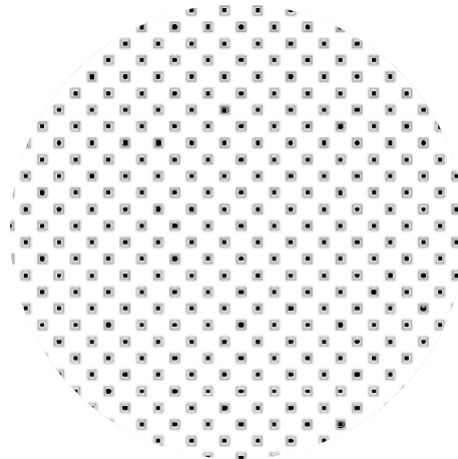
Figure 3.41: OCT-00 geometry: filter structure.

44

3.3.2 Lifetime study

Testing conditions, described in Section 2.4, provide conclusions here presented. Focusing on the pressure drop of the filter, in this section lifetime is analyzed in terms of time to get $150mbar$ (s) inlet/outlet of the filter. It is analyzed how the lifetime changes with the filter density. This analysis is here divided and analyzed for each geometry.

SQR geometry, as already explained in Section 2.5, is one of the most used on the market nowadays (12). Figure 3.42 shows the results obtained for the testing conditions #1. It underlines the trend already investigated in Figure 3.36-3.37, decreasing the wall thickness to the outlet, SQR geometry increases the lifetime.
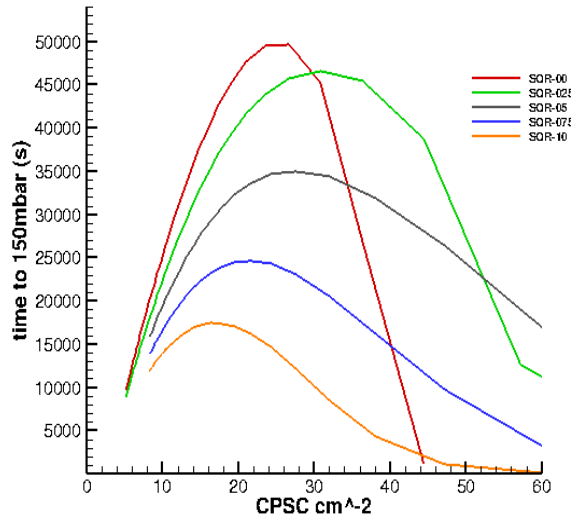
Figure 3.42: SQR geometry: results for test conditions # 1.

Maximum results are obtained for SQR-00 geometry. Meaning, for proportion and design of this geometry, the greater the inlet channel area the bigger the lifetime. This conclusion is also underlined by looking at the worse results of the geometry, they occur for SQR-10. In Tab. 3.8 the maximum values for the analysis are sum up.

Geometry	$CPSC\ [cm^{-2}]$	$A_e\ [m^2]$	Lifetime $[s]$	r_{12}	r_{wp}
$SQR-00$	26.67	7.50×10^{-6}	49680.0	3.26	2.82
$SQR-025$	30.77	6.50×10^{-6}	46650.0	1.89	2.49
$SQR-05$	27.59	7.25×10^{-6}	35040.0	1.0	2.19
$SQR-075$	21.62	9.25×10^{-6}	24690.0	0.60	1.98
$SQR-10$	16.33	1.225×10^{-5}	17460.0	0.420	1.84

Table 3.8: Maximum values for SQR geometry analysis: testing conditions #1.

TRI geometry reveals a similar trend compared with SQR geometry. It, in fact, affirms the tendency analyzed in Figures 3.36-3.37. Figure 3.43 shows the results of the investigation. By comparing these results with the SQR results, it is possible to see a close similarity.
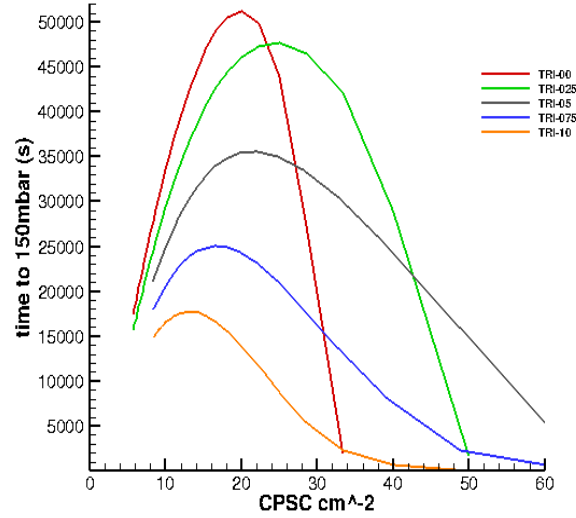
Figure 3.43: TRI geometry: results for test conditions # 1.

Maximum results are obtained for TRI-00, while the worse ones occur for TRI-10. The maximums of the curves occur in a constant CPSC range. If comparing this range, it corresponds to the commercial range of filters on market. In Table 3.9 maximums for each curve are sum up.

Geometry	$CPSC\ [cm^{-2}]$	$A_e\ [m^2]$	Lifetime $[s]$	r_{12}	r_{wp}
$TRI-00$	20.00	1.0×10^{-5}	51150.0	3.18	3.22
$TRI-025$	25.00	8.0×10^{-6}	47640.0	1.93	2.82
$TRI-05$	21.98	9.1×10^{-6}	35640.0	1.0	2.47
$TRI-075$	16.53	1.21×10^{-5}	25050.0	0.60	2.26
$TRI-10$	13.33	1.5×10^{-5}	17730.0	0.41	2.07

Table 3.9: Maximum values for TRI geometry analysis: testing conditions #1.

HEX-TRI geometry, as illustrated in Figure 3.36, shows an opposite trend to the wall thickness asymmetric distribution. Figure 3.44 shows the results for testing conditions #1.
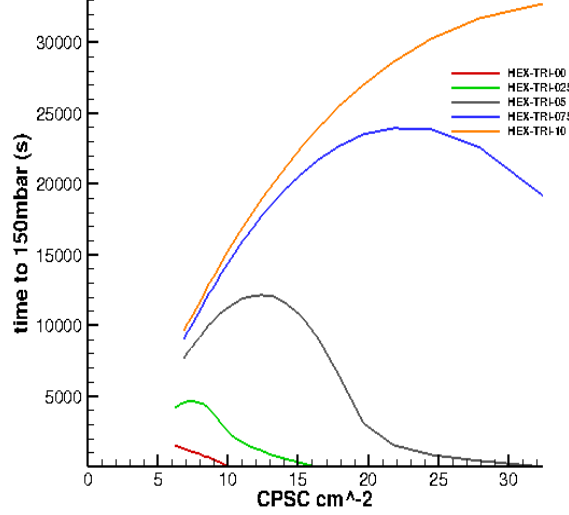
Figure 3.44: HEX-TRI geometry: results for test
conditions # 1.

Compared to SQR and TRI, the trend is the opposite. For the same wall thickness distribution, the results are not comparable with the corresponding equal f_1 geometry of the other cases. The maximum lifetime occurs for HEX-TRI-10, while HEX-TRI-00 becomes the worst case. Furthermore, curves are stopped for low values of CPSC; even if some of them seems growing up, investigating very low CPSC is not in concordance with the actual values of filter density on the market. In Table 3.10 the maximums are sum up. By analyzing these values it is possible to see as, good results are achieved only for HEX-TRI-10 geometry, the other cases show very short lifetime. It is interesting to check values of r_{12}, for many cases the value is really big.

Geometry	$CPSC$ $[cm^{-2}]$	A_e $[m^2]$	Lifetime $[s]$	r_{12}	r_{wp}
$HEX - TRI - 00$	6.19	4.85×10^{-5}	1460.0	8.33	3.22
$HEX - TRI - 025$	7.32	4.1×10^{-5}	4640.0	6.11	3.11
$HEX - TRI - 05$	12.37	2.425×10^{-5}	12160.0	4.77	2.92
$HEX - TRI - 075$	21.82	1.375×10^{-5}	23980.0	3.0	2.62
$HEX - TRI - 10$	32.43	8.5×10^{-6}	32770.0	1.45	2.24

Table 3.10: Maximum values for HEX-TRI geometry analysis: testing conditions #1.

OCT geometry has a similar trend compared with HEX-TRI geom-

etry. This, in fact, is adopted to provide a bigger inlet channel area and area for the cake to grow up at the same time. Figure 3.45 shows the results of the analysis. The trend is similar to HEX-TRI geometry (see Figure 3.44), but in this case, for the CPSC range analyzed, some geometries are free to be fully developed: meaning showing a maximum along the range.
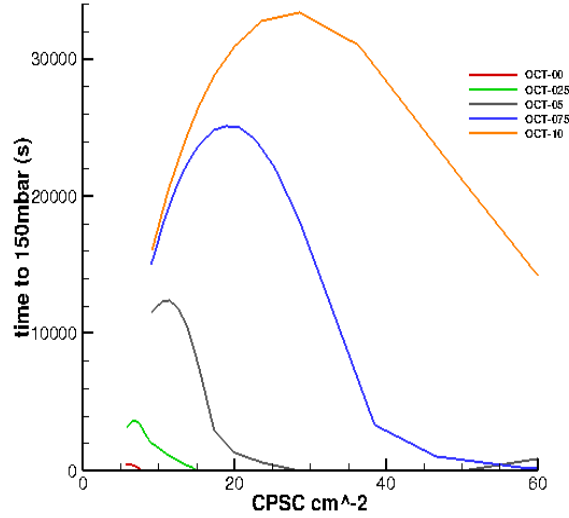
Figure 3.45: OCT geometry: results for test conditions # 1.

In Table 3.11 the maximum values are resumed. As for HEX-TRI geometry, r_{12} OCT geometry values are really big. It highlights the design criteria of this geometry: bigger inlet channel area.

Geometry	$CPSC\ [cm^{-2}]$	$A_e\ [m^2]$	Lifetime $[s]$	r_{12}	r_{wp}
$OCT-00$	5.71	7.0×10^{-5}	480.0	11.5	2.34
$OCT-025$	6.90	5.8×10^{-5}	3610.0	8.87	4.5
$OCT-05$	11.43	3.5×10^{-5}	12390.0	6.86	4.2
$OCT-075$	18.87	2.12×10^{-5}	25130.0	4.4	3.75
$OCT-10$	28.57	1.40×10^{-5}	33380.0	2.19	3.16

Table 3.11: Maximum values for OCT geometry analysis: testing conditions #1.

HEX geometry shows a trend similar to SQR and TRI. Figure 3.46 shows the results. For testing conditions #1, these are the best results. Each geometry is fully developed along the CPSC range investigated. As described in Section 3.3.1, HEX-00 and OCT-00 geometries follow a different trend since they come from limit cases.
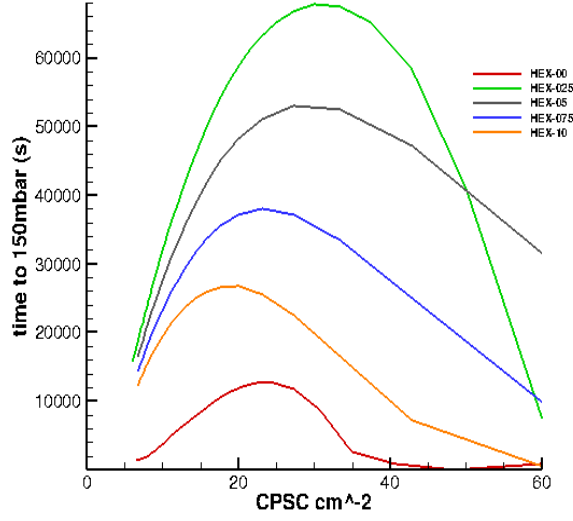
Figure 3.46: HEX geometry: results for test conditions # 1.

Table 3.12 shows the maximum values occurring for the geometry.

Geometry	$CPSC\ [cm^{-2}]$	$A_e\ [m^2]$	Lifetime $[s]$	r_{12}	r_{wp}
$HEX - 00$	24.59	1.22×10^{-5}	12700.0	5.51	2.15
$HEX - 025$	30.00	1.0×10^{-5}	67770.0	3.52	3.82
$HEX - 05$	27.27	1.1×10^{-5}	52980.0	2.0	3.4
$HEX - 075$	23.08	1.30×10^{-5}	38010.0	1.24	3.05
$HEX - 10$	20.00	1.50×10^{-5}	26700.0	0.83	2.75

Table 3.12: Maximum values for HEX geometry analysis: testing conditions #1.

Second testing condition results are provided in this section. The reader is referred to Section 2.4 for the detailed description of the parameters. This condition depicts a slower loading filter condition.

SQR geometry is investigated in all the cases as well. Figure 3.47 shows the results for this case. The results are in concordance with the results for testing conditions #1. SQR-00 is the best geometry in terms of lifetime, the advantage of this geometry is affirmed over the filter density range analyzed.
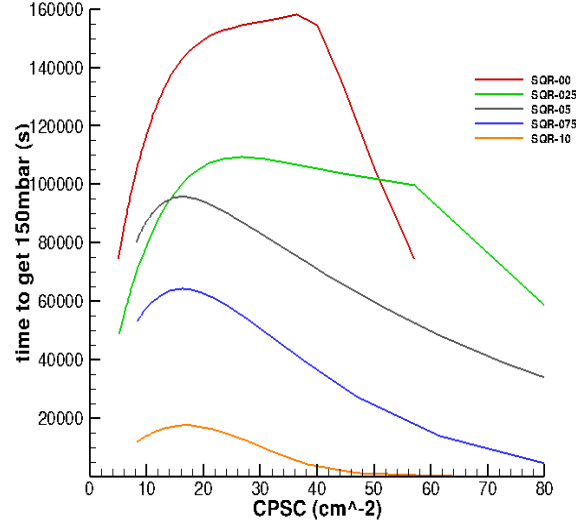
Figure 3.47: SQR geometry: results for test conditions # 2.

In Table 3.13 the maximum values are shown. The difference between high r_{12} value and low r_{12} value is relevant. SQR-10, in fact, provides incomparable results.

Geometry	$CPSC \ [cm^{-2}]$	$A_e \ [m^2]$	Lifetime $[s]$	r_{12}	r_{wp}
$SQR-00$	36.36	5.5×10^{-6}	158070.0	4.35	2.82
$SQR-025$	26.67	7.5×10^{-6}	109470.0	1.79	2.51
$SQR-05$	16.33	1.225×10^{-5}	95760.0	1.0	2.33
$SQR-075$	16.33	1.225×10^{-5}	64260.0	0.65	2.09
$SQR-10$	16.33	1.225×10^{-5}	17460.0	0.42	1.84

Table 3.13: Maximum values for SQR geometry analysis: testing conditions #2.

Results for TRI geometry are shown in Figure 3.48. These results are similar to the SQR geometry ones. TRI-10 shows results incomparable with the other geometries investigated. TRI-00 provides the best geometry over a large range of filter density. In Table 3.14 the maximum results for each geometry are reported.
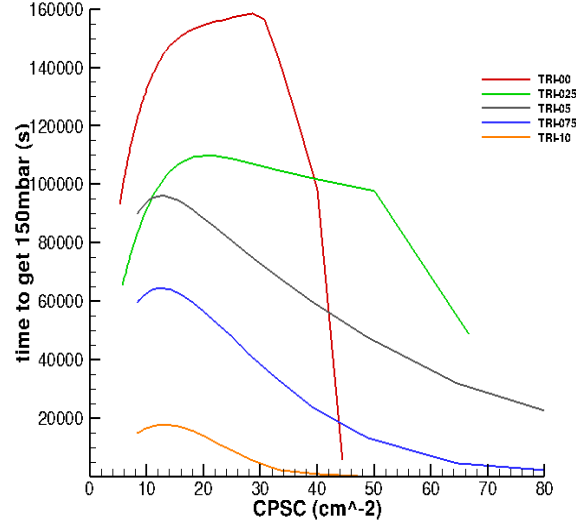
Figure 3.48: TRI geometry: results for test conditions # 2.

Geometry	$CPSC\ [cm^{-2}]$	$A_e\ [m^2]$	Lifetime $[s]$	r_{12}	r_{wp}
$TRI-00$	28.57	7.0×10^{-6}	158670.0	4.46	3.22
$TRI-025$	20.00	1.0×10^{-5}	109890.0	1.77	2.87
$TRI-05$	12.42	1.61×10^{-5}	96030.0	1.0	2.66
$TRI-075$	12.42	1.61×10^{-5}	64500.0	0.66	2.38
$TRI-10$	13.33	1.5×10^{-5}	17730.0	0.41	2.07

Table 3.14: Maximum values for TRI geometry analysis: testing conditions #2.

HEX-TRI geometry, as discussed in Section 3.3.1, could give different output at different wall thickness distribution. This case is different from the other for some details. Figure 3.49 could help to understand the uniqueness of this case. While the other geometries show a trend changing from a value of f_1 to another one, HEX-TRI for testing condition #2 creates a peak. Starting from $f_1 = 0.0$, the lifetime of the geometry initially increases, then reaching $f_1 = 0.5$ it decreases. That is the reason why HEX-TRI-075 and HEX-TRI-10 show less significant results. To better understand the values of this test, Table 3.15 sum up the maximum values for each geometry.

Figure 3.49: HEX-TRI geometry: results for test conditions # 2.

Geometry	$CPSC\ [cm^{-2}]$	$A_e\ [m^2]$	Lifetime $[s]$	r_{12}	r_{wp}
$HEX - TRI - 00$	9.84	3.05×10^{-5}	71160.0	12.30	3.22
$HEX - TRI - 025$	15.38	1.95×10^{-5}	89490.0	9.75	3.05
$HEX - TRI - 05$	26.09	1.15×10^{-5}	143970.0	6.42	2.78
$HEX - TRI - 075$	27.27	1.1×10^{-5}	130600.0	3	2.55
$HEX - TRI - 10$	27.27	1.1×10^{-5}	91470.0	1.56	2.32

Table 3.15: Maximum values for HEX-TRI geometry analysis: testing conditions #2.

OCT geometry, similar to HEX-TRI, does not show a unique trend by changing the wall thickness distribution. In Figure 3.50 is possible to see the results for testing condition #2. The maximum value is reached for OCT-025. The trend is; increasing lifetime until OCT-025 then decreasing. in Table 3.16 the maximum values for all the geometries investigated are shown.
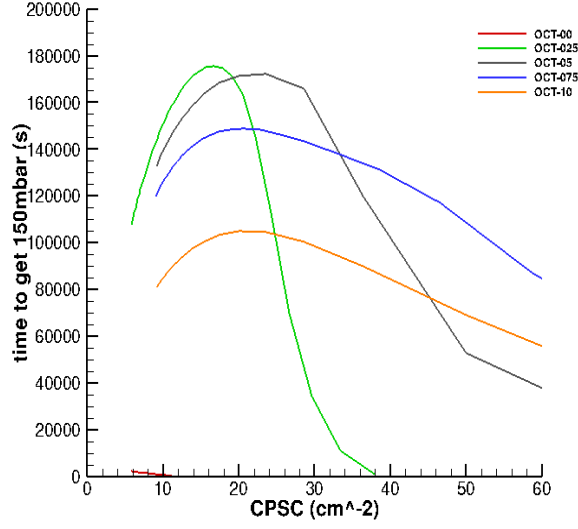
Figure 3.50: OCT geometry: results for test conditions # 2.

Geometry	$CPSC$ $[cm^{-2}]$	A_e $[m^2]$	Lifetime $[s]$	r_{12}	r_{wp}
$OCT-00$	10.53	3.8×10^{-5}	28620.0	17.6	2.34
$OCT-025$	16.67	2.40×10^{-5}	175710.0	14	4.4
$OCT-05$	23.53	1.7×10^{-5}	172380.0	8.46	4.0
$OCT-075$	20.62	1.94×10^{-5}	148990.0	4.37	3.71
$OCT-10$	20.00	2.0×10^{-5}	105030.0	2.55	3.41

Table 3.16: Maximum values for OCT geometry analysis: testing conditions #2.

Last geometry investigated is HEX. It shows the same trend already seen for testing conditions #1. Figure 3.51 shows the resulting curves. The best results occur for small wall thickness fraction to the inlet side. This result specifically, depicts as the best geometry HEX-025. The results are sum up in Table 3.17. As said before, HEX-00 is not shown since it represents a limita case of the actual thickness wall distribution strategy (see Figures 3.38-3.39).
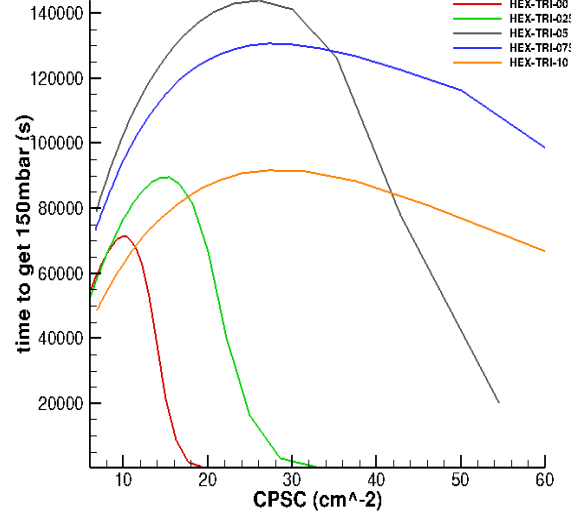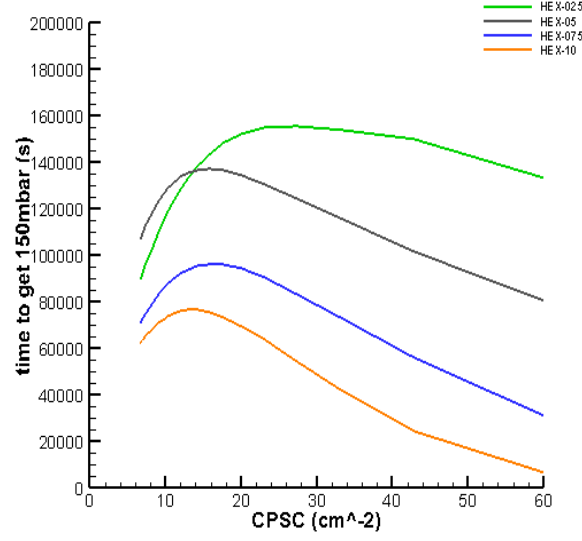
Figure 3.51: HEX geometry: results for test conditions # 2.

Geometry	$CPSC\ [cm^{-2}]$	$A_e\ [m^2]$	Lifetime $[s]$	r_{12}	r_{wp}
$HEX-00$	40.54	7.4×10^{-6}	192870.0	8.44	2.15
$HEX-025$	27.27	1.1×10^{-5}	155730.0	3.40	3.85
$HEX-05$	15.79	1.9×10^{-5}	137610.0	2.00	3.61
$HEX-075$	15.79	1.9×10^{-5}	96390.0	1.37	3.27
$HEX-10$	14.29	2.1×10^{-5}	76680.0	0.97	3.0

Table 3.17: Maximum values for HEX geometry analysis: testing conditions #2.

Once testing conditions are studied for all the geometries investigated, it is possible to analyze the results comparing all the geometries. This analysis is carried out in order to obtain a general comparison among all the geometries and getting out some conclusions. This analysis takes into account the best geometries in terms of lifetime. These geometries are the same already investigated above. According to testing condition # 1, Figure 3.52 shows a correlation among them.
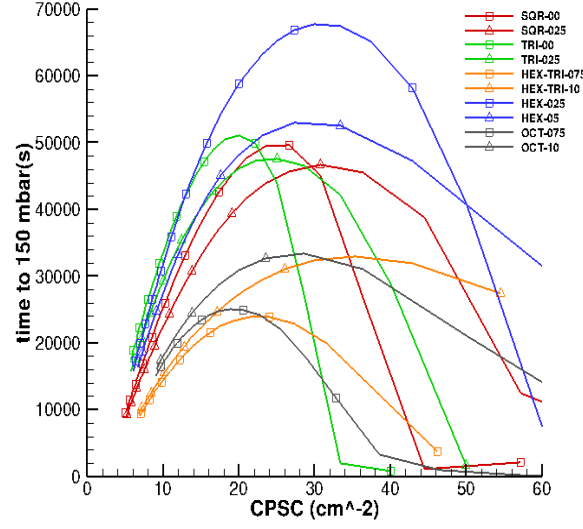
Figure 3.52: Analysis of best lifetime geometries: results
for test conditions # 1.

Same colors indicate same basis geometries, different labels on lines indicate different geometries (in terms of f_1 values). Best results are obtained, for testing condition # 1, with HEX-025 and HEX-05 geometry. Specifically, HEX-025 could reach a gain of 28% respect to HEX-05. The combination of open frontal area and area for the cake to grew up leads to higher results compared with the others. As seen above, TRI and SQR show similar trends comparing lifetimes even if the curves are not exactly the same. In fact, maximums are more or less equal; SQR-00 maximum lifetime value is 2.8 % less than corresponding maximum for TRI-00, a smaller difference is obtained between SQR-025 and TRI-025 geometries. On the other hand, the maximums, for SQR and TRI, occur for different filter densities (CPSC: for SQR-00 26.67, for TRI-00 20.0). Different from SQR and TRI, HEX-00 and HEX-025 geometries develop a flat maximum offering high lifetimes over a large filter density range. HEX-TRI and OCT geometries depict a different scenario. For testing condition # 1, their results are not comparable with the previous geometries cited above. Even if maximums (for OCT-075, OCT-10, HEX-TRI-075 and HEX-TRI-10) occur in the same filter range, the results are not even close to the HEX, SQR and TRI ones. Specifically OCT-10 maximum is 50% less than HEX-025 maximum, while HEX-TRI-10 is 52% less than the same one. The reason has to be recognized in the design of the geometries. The inlet/outlet area ratio is different from the previous geometries and, specifically, the outlet channel, is too small. This leads

to higher velocities and higher pressures in the outlet channels.

The same comparison is here provided for testing conditions # 2. This analysis takes into account the best geometries in terms of lifetime. Analyzed geometries are the same already investigated above. According to testing condition # 2, Figure 3.53 shows a correlation among them.
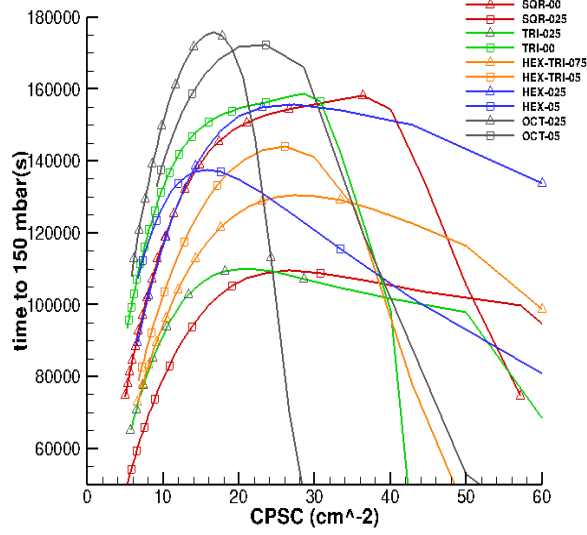
Figure 3.53: Analysis of best lifetime geometries: results for test conditions # 2.

The scenario here depicted, is different from the one illustrated in Figure 3.52. While the previous analysis demonstrates a clear difference among different geometries, testing conditions # 2 manifest a different situation. OCT-05 and OCT-025 are the best results for this case. Despite a different f_1 value, these geometries carry out two similar maximum values, in fact, OCT-025 is only 1,8% more than OCT-05. The curves are less flat than the others, this leads to a superiority in a small filter density range. TRI-00, SQR-00 and HEX-025 show similar trends. The Maximums are similar (difference: SQR-00/TRI-00 is 0.4%, HEX-025/TRI-00 is 1.8%) and the curves similarly develop on the filter density range investigated.

Constantly smaller results are obtained for HEX-TRI geometry (for both 0.75 and 0.5 f_1 values). Along the work, it has been often underlined the similarities between HEX-TRI and OCT. Even if, for testing conditions # 1, OCT geometry shows better results, HEX-TRI does not work in the same direction. The reason has to be associated with the inlet/outlet ratio and to the ratio perimeter/area of the geometries.

3.3.3 Pressure drop analysis

The pressure drop across the Diesel Particulate Filter (DPF) is one of the most important critical parameters in the design of a DPF regeneration strategy. When the pressure drop is too high, there is a significant amount of particulate accumulated on the filter wall. If the DPF is regenerated, there may be a large heat release which may cause a crack in the DPF. Also, the additional particulate needs more thermal energy to complete the regeneration. This energy is often provided by combustion diesel fuel, which leads to a lower fuel economy, which is an issue that should be considered at the same time. The total pressure drop of the filter channel can be divided into four parts: inlet channel pressure drop, pressure drop across the soot deposit, pressure drop across the substrate wall and outlet channel pressure drop (32).

There are several critical parameters in the pressure drop models. These include the inlet temperature and gas flow rate, which are two operating parameters depending on the exhaust gases conditions, while the filter wall thickness is a design parameter which cannot be changed. Wall thickness, according to Section 2.4, it is set to t_{wall} 431.8×10^{-6} m. The inlet temperature (T_{gas}) is 533.0 K, while the gas flow rate depends on the testing conditions (#1 or #2).

Keeping in consideration the maximums values occurring from the previous investigations, in this section, the pressure drop evolution is shown for each investigated geometry. Models are shown in terms of:

- pressure drop inlet/outlet of the filter. The model does not take into account turbulence effects or disruptions at the inlet/outlet of the filter;

- soot collected in the filter. This measure, as usual in literature, is a volumetric quantity.

As explained in Section 3.3.2, the simulations are carried out by setting a maximum value to pressure drop inlet/outlet of the filter. This value is set to 150 mbar. This leads to indirectly obtain the quantity of soot accumulated in the filter.

Figure 3.54 illustrates the pressure drop evolution for best lifetime geometries according to testing conditions #1 (results showed in Figure 3.52). The x-axis is limited to 12 kg/m^3 since a higher collected soot in filter level may be extreme. Regeneration is not included in the present

work but, according to literature works (33; 34), a maximum value for collected soot in filter level is set to 12 kg/m^3.
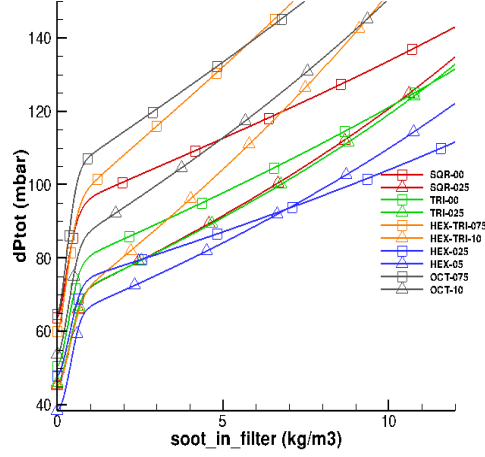
Figure 3.54: Pressure drop evolution for geometries showed in Figure 3.52.

From Figure 3.54 many conclusion are obtainable. HEX-TRI-075 and OCT-075 show a big initial pressure drop due to the relevant asymmetric design of the inlet and outlet cells. HEX-TRI-10 and OCT-10 although the initial pressure drop is not huge, the deep bed filtration slope rises up, this leads a quickly increases of the accumulated soot level. To better visualize the initial stage of the process, Figure 3.55 is provided. There is a range of 30 *mbar* from the lowest initial pressure drop to the highest one.

Figure 3.55: Pressure drop evolution for geometries showed in Figure 3.52: focus on the initial pressure drop.

According to the previous conclusions, SQR, TRI and HEX provide the best results. The initial pressure drop of SQR-00 is bigger due to the higher r_{12} value, then it develops with a lower slope during cake formation stage compared to TRI geometry. SQR-025 shows a smaller initial pressure drop, then it develops like TRI-025 geometry. HEX-025 and HEX-05 show over the almost entire range a lower pressure drop development. Figure 3.56 highlights SQR,TRI and HEX pressure drop evolution. The relationship between HEX-025 and HEX-05 needs particular attention. Although the initial pressure drop is bigger for HEX-025, switching to cake formation stage, it gives better results from a certain soot in filter level (around 7 kg/m^3). Due to this intersection, no more conclusions are detectable, since adopting one geometry instead of another depends on the regeneration strategy of the engine. In fact, depending on the soot in filter level, regeneration affects the peak temperature in the filter which is limited by the thermal resistance of the filter adopted.

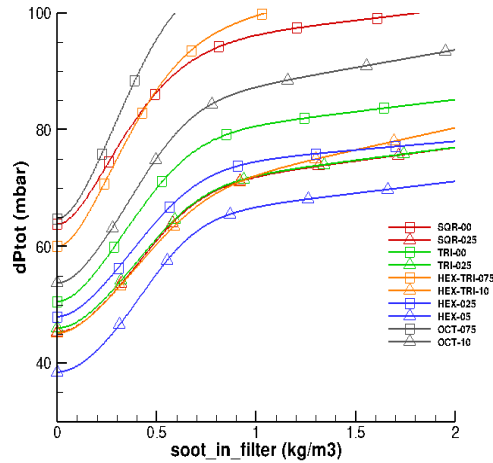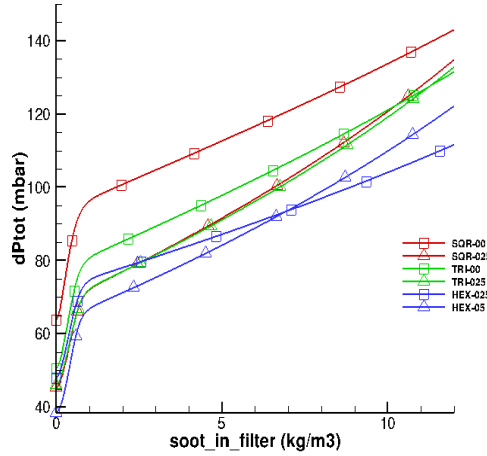Figure 3.56: Pressure drop evolution for geometries showed in Figure 3.52: focus SQR,TRI and HEX geometries.

A similar comparison is provided for testing conditions # 2. For specific testing conditions, the reader is referred to Section 2.4. Figure 3.57 illustrates the pressure drop evolution for the best lifetime geometries according to testing conditions # 2. Maximum x-axis value is set to 12 kg/m^3.

Differently from testing conditions # 1, pressure drop model evolves reaching the non-linear status of the cake growth stage. This non-linear behaviour, reached before 12 kg/m^3, impacts on the performances of the

DPF geometries and on the choice of the best DPF geometry for these conditions. In fact, if choosing a different soot in filter limit to start the regeneration, the pressure drop reached during this phase changes.
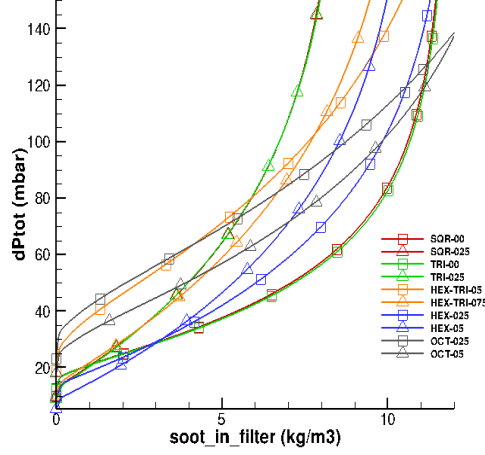
Figure 3.57: Pressure drop evolution for geometries showed in Figure 3.53.

OCT geometries are the ones that keep the linear behaviour during the entire process. This effect allows the geometries to demonstrate good results in terms of pressure drop reached for high soot in filter levels. Anyway, other geometries show better results during the process but they reveal a non-linear behaviour in the last phase which affects the pressure drop. Specifically, SQR-00, TRI-00, HEX-025 and HEX-05 evolve with a lower slope until non-linear behaviour occurs. If choosing a smaller collected soot in filter value, the advantages of the previous geometries may be bigger than the other ones.

Furthermore in Figure 3.58, the initial pressure drop, occurring for best lifetime geometries, according to testing conditions # 2, is showed. By comparing these results and the previous ones in Figure 3.55, it is clear as OCT and HEX-TRI always provide higher initial pressure drop due to greater inlet/outlet areas ratio. On the other hand, HEX, SQR and TRI geometries provide better initial pressure drop values.
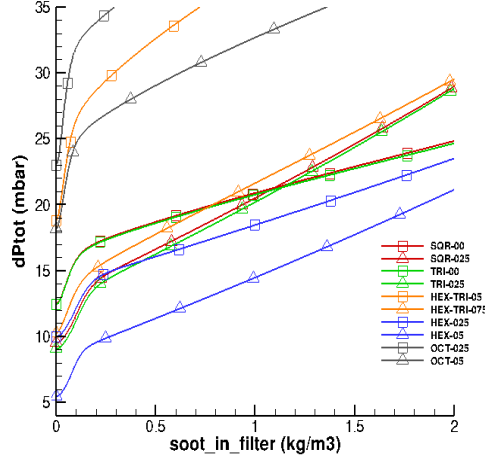
Figure 3.58: Pressure drop evolution for geometries
showed in Figure 3.53: focus on the initial pressure drop.

3.3.4 Efficiency analysis

Using the same testing conditions presented in Section 2.4, here it is
presented the different behaviour of the geometries in terms of time to
reach 100% efficiency starting from clean filter conditions.
The time to reach 100% efficiency is directly connected with PM emis-
sions. As mentioned in Section 1.2.2, PM is mostly trapped at the wall
surface of the DPF and is deposited on the wall by forming the layer.
The filtration efficiency becomes close to 100% after a certain thickness
of this soot layer is formed. This happens since the formed soot layer
plays a role in trapping the soot which is coming from the exhaust man-
ifold of the engine. If trapping the soot on the surface, it cannot flow
through the wall escaping from the filter. For this reason, the period
to reach 100% efficiency plays an important role in measuring the PM
entirely escaping from the filter (35).

   The analysis has the objective to show the differences among the
investigated geometries. The conditions accord with the ones used to
detect the lifetime. The study takes into account only one particle size
of PM ($d_{part} = 180.0 \times 10^{-9}$ m). This size is recognized, in literature, as
in the range of the difficult particles to collect; these are very important
since more dangerous for human health.

   The analysis is carried out one for each geometry investigated. For
SQR and TRI geometry the results are sum up respectively in Figures
3.59-3.60. These results are obtained according to testing conditions #
1.

Figure 3.59: SQR geometry: time to reach 100% efficiency according to test conditions # 1.

Figure 3.60: TRI geometry: time to reach 100% efficiency according to test conditions # 1.

By comparing the previous figures, it is clear as the two geometries depict similar scenes. Since the usage filter density range is $[10; 25]$ cm^{-2} the differences in this range are not so relevant. This underlines that, choosing one filter wall distribution rather than another one, does not give relevant advantages from the filtration efficiency point of view.

Similar scenario is depicted for the other geometries (see Figures 3.61-3.62-3.63). It is clear HEX-TRI, OCT and HEX do not cover the entire filter density range; it happens due to the strong asymmetric design for certain f_1 values where small periodic element area (meaning bigger CPSC values) occurs. Different from what underlined before, in these cases over the usual filter density range ($[10; 25]$ cm^{-2}), HEX-TRI and OCT geometries (symmetric and asymmetric designs) show relevant differences from one f_1 values to another one. This does not happen for HEX geometry, where the differences remain small (around 0.5 hours).
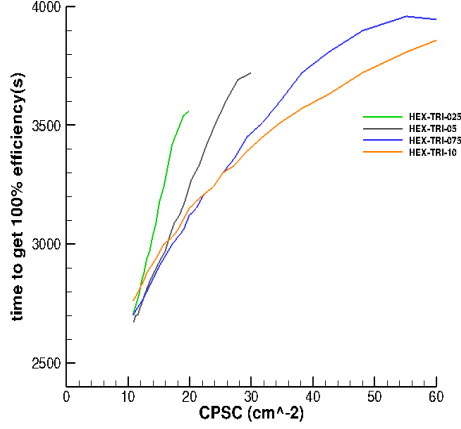
Figure 3.61: HEX-TRI geometry: time to reach 100% efficiency according to test conditions # 1.
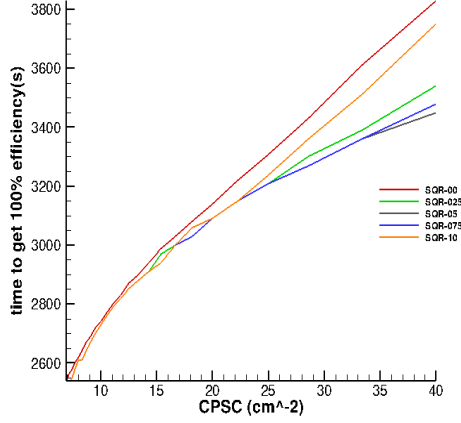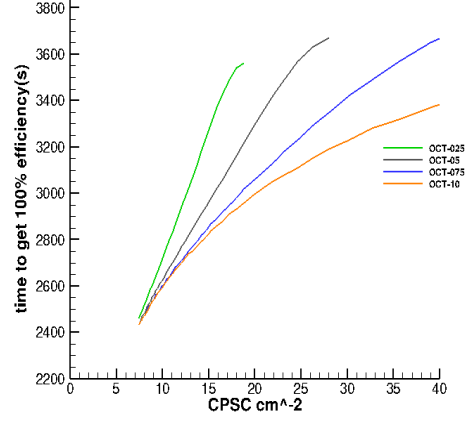

Figure 3.62: OCT geometry: time to reach 100% efficiency according to test conditions # 1.

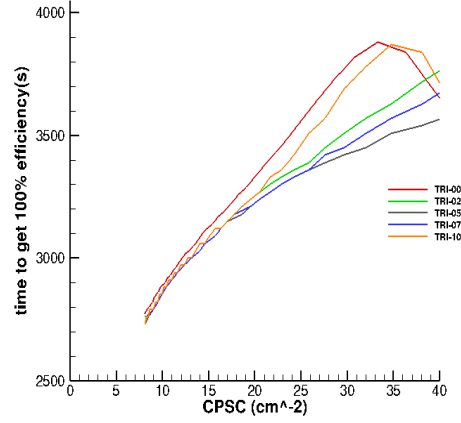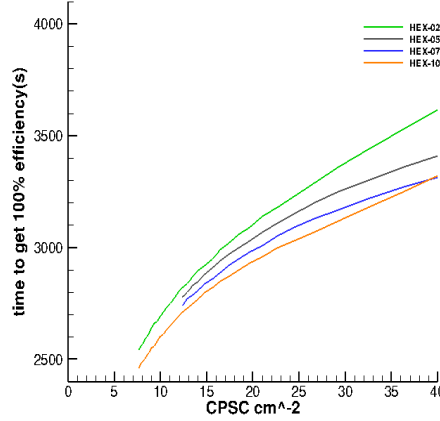Figure 3.63: HEX geometry: time to reach 100% efficiency according to test conditions # 1.

The efficiency detection of the investigated geometries has the objective to highlight the differences if choosing one geometry instead of another one. For this reason Table 3.18 shows a comparison among the investigated geometries for an equal filter density (CPSC). Specifically, it is chosen a filter density of 20 CPSC (cm^{-2}), this means a filter density of $\simeq 130$ CPSI (in^{-2}). Analyzing this table it is possible to obtain the maximum and minimum value for the filter density analyzed:

- Max: 3600 s;

- Min: 2940 s;

It means the range is 660 s (around 11 min).

	Geometry	Time to 100 % efficiency [s]
SQR	SQR-00	3140
	SQR-025	3090
	SQR-05	3090
	SQR-075	3090
	SQR-10	3090
TRI	TRI-00	3330
	TRI-025	3260
	TRI-05	3240
	TRI-075	3230
	TRI-10	3260
HEX-TRI	HEX-TRI-025	3560
	HEX-TRI-05	3260
	HEX-TRI-075	3120
	HEX-TRI-10	3150
HEX	HEX-025	3100
	HEX-05	3040
	HEX075	3000
	HEX-10	2940
OCT	OCT-025	3600
	OCT-05	3350
	OCT-075	3070
	OCT-010	3010

Table 3.18: Time to get 100% efficiency for $CPSC = 20cm^{-2}$: testing conditions #1.

Furthermore, another Table is presented in order to better understand the differences. Table 3.19 shows the results of the investigation. Many geometries do not show their results, in fact, for CPSC 30 (cm^{-2}), considering the wall thickness used, not all the geometries generates comparable and consistent results. This happens mainly due to the illogical divergence between inlet and outlet areas . A filter density of 30 CPSC (cm^{-2} corresponds to a filter density of $\simeq 200$ CPSI (in^{-2})
Analyzing this table it is possible to obtain the maximum and minimum value for the filter density analyzed:

- Max: 3810 s;

- Min: 3130 s;

It means range is 680 s (around 11 min).

	Geometry	Time to 100 % efficiency [s]
	SQR-00	3500
	SQR-025	3350
SQR	SQR-05	3300
	SQR-075	3330
	SQR-10	3400
	TRI-00	3810
	TRI-025	3550
TRI	TRI-05	3430
	TRI-075	3480
	TRI-10	3710
	HEX-TRI-05	3720
HEX-TRI	HEX-TRI-075	3470
	HEX-TRI-10	3400
	HEX-025	3370
HEX	HEX-05	3270
	HEX075	3200
	HEX-10	3130
	OCT-05	3700
OCT	OCT-075	3420
	OCT-010	3230

Table 3.19: Time to get 100% efficiency for $CPSC = 30cm^{-2}$: testing conditions #1.

3.3.5   General geometry study

During the operation of the filter, soot and ash are accumulated within the walls and inside the inlet channels. The deposited soot is removed during filter regeneration (continuously or periodically). The ash, on the other hand, remains in the filter causing a gradual irreversible increase of the filter pressure drop. Once the pressure drop builds up to an unacceptably high level, the filter must be either cleaned or replaced with a new unit. At a given level of ash emission (from the lube oil additives, fuel additives, etc.), the ash storage capacity can be increased by either using a larger size substrate or else by designing the substrate to provide more volume on the upstream (inlet) side of the monolith. The latter asymmetric design would provide a greater surface area for storing the ash, leaving the ash-filled inlet channels more open in comparison to the conventional design.

Working on some geometries has demonstrated advantages and disadvantages in specific exhaust gas conditions. Literature has tried for many years to introduce and study the improvements of some geometries instead of other ones. For example, Majewski et al. (5), have tried to study many symmetric and asymmetric geometries proposed by the lit-

erature. Some of them really began to be commercialized, many others have reflected their inconsistency. Due to the model generic approach to the geometries, this section describes a new method to investigate different geometries. Diesel particulate filter lifetime could be controlled by the design criteria of the filter, apart from materials and others aspect, the design plays an important role. From this point of view, the crucial parameters are A_e, f_1, r_{120} and r_{wp0} (see Section 2.4). By keeping in mind a general geometry, without referring to any specific geometry, an investigation is done using combination of A_e, f_1, r_{120} and r_{wp0}. This means investigating geometries maybe not known or even not real, but also, for example, the already studied geometries. This could give an idea of what could be done to improve diesel particulate filter lifetime or how good are the geometries used compared to others not even introduced.

This study is carried out according to testing conditions # 1 (see Section 2.4), that are closer to real driving conditions. Simulation is performed adopting the following assumptions:

- Darcy friction factor corresponds to the circle geometry;

- the general geometry is assumed to have two cells for each periodic element;

- the geometrical relationships follow Equations 2.1-2.2.

Since Darcy factor depends on the geometry and since no geometry is referred to this analysis, it has been chosen a circular geometry. Furthermore, since no geometry is referred to this analysis, a number of two cells for the periodic element is chosen.

Figure 3.64 shows a qualitative comparison obtained analyzing a general unknown geometry. Main parameters of the analysis are sum up in Table 3.20. The main geometries analyzed along the work are shown as well. Furthermore lines in figure, represent Φ_1.

Figure shows that there is a specific trend in terms of Φ_1, when it is in the range $0.3 \div 0.55$, it implies better results in terms of geometry lifetime. The geometries investigated depicts the lower side of the graph, there are no investigations for the upper side of the graph.
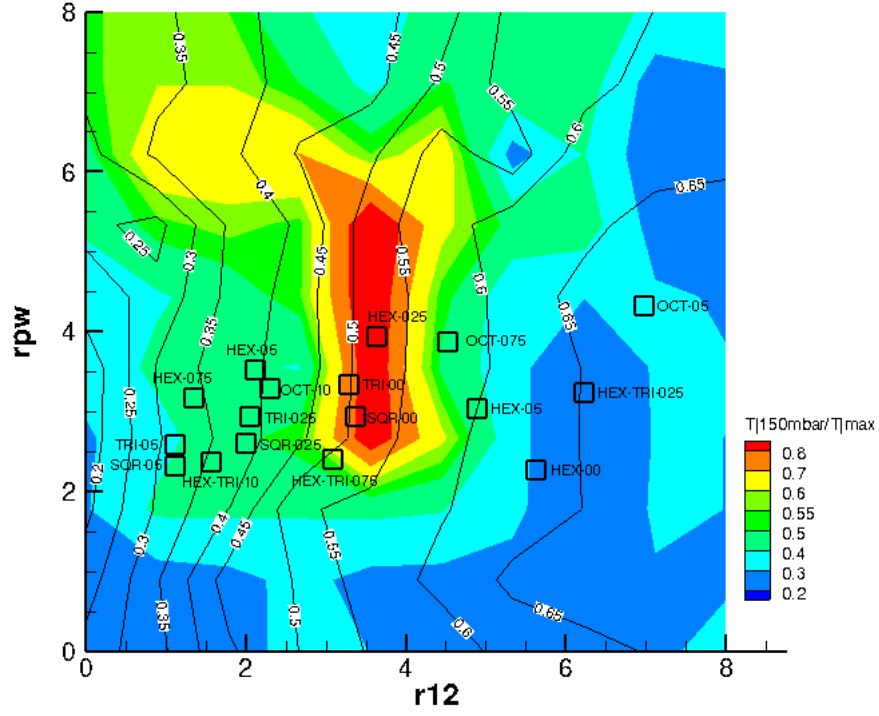
Figure 3.64: Generic geometry study: qualitative comparison.

Parameter	Value/Range
t_{wall} (μm)	431.8
r_{120}	$0.5 \div 8.0$
r_{wp}	$0.5 \div 8.0$
A_e (m^2)	$5.0 \times 10^{-6} \div 33.0 \times 10^{-6}$

Table 3.20: Generic geometry study: parameters.

67

Conclusion

In this work, it has been investigated a new DPF numerical model based on a general geometry approach. For specific testing conditions several geometries were tested, furthermore, due to a specific wall thickness distribution strategy, new geometries are tested. The results, comparing several geometries, have demonstrated advantages/disadvantages of some geometries compared to others. By checking the two testing conditions examined in the work, HEX geometry provides better results in terms of lifetime. This conclusion is confirmed in literature ((5; 28; 36; 29)). On the other hand, HEX-TRI, which is an experimental geometry, does not show relevant geometry; conclusion also affirmed in literature (5)). This conclusion has been reached by comparing the two model testing conditions. SQR and TRI geometries are really similar and the advantages/disadvantages of one compared to the other, are not relevant. They proceed similarly for both testing conditions. In terms of comparison with the other geometries, SQR and TRI results are slightly smaller but comparable with the HEX results. OCT geometry shows good results only with testing conditions # 2. It works better with slower flow rate, when increasing the flow rate, OCT geometry quickly develop a pressure drops peak due to its design (low open area of outlet channels). For this reason, OCT geometry could provide good results only for specific applications; for example coupling this geometry for engines that provide a slower exhaust gas flow rate. There are no huge advantages from the efficiency point of view, the differences remain in a tolerable range without affecting the already optimal filter efficiency.

The generic geometry study leads to global conclusions. There is a combination of geometric values where some geometries, even without referring to a specific shape, show better lifetimes. It can be seen in the opposite terms; far from these best working conditions, some geometries reveal inconsistent results. This perspective could be seen if looking at the geometric parameters of some unsatisfactory geometries (HEX-TRI for example). Figure 3.64, according to the testing conditions analyzed,

could be seen as a reference to recognize if a specific geometry could give good results or if it could be improved geometrically.

According to Archimedean tilings, many other geometries could be investigated (see Figure 4.65). The point of view of this work underlines the importance of the geometry design admitting the existence of geometrical parameters ranges where some geometries could provide better results. This criterion has been validated and confirmed along the work by comparing several designs. Many symmetric or asymmetric tiling geometries have never been investigated. The technological improvements in the additive manufacturing field, could provide an easy access to some geometrical designs before forbidden by the classic manufacturing processes. These improvements could provide the best materials and the best geometries that, probably, have not yet been found out.

Figure 4.65: Asymmetric cell designs.

Bibliography

[1] Ali Keskin İbrahim Aslan Reşitoğlu, Kemal Altinişik. The pollutant emissions from diesel-engine vehicles and exhaust aftertreatment systems. *Clean Technologies and Environmental Policy*, 17:15–27, 2015.

[2] Joshua Miller and Lingzhi Jin. Global progress toward soot-free diesel vehicles in 2018. *Climate and Clean Air Coalition to Reduce Short-Lived Climate Pollutants (CCAC)*, 2018.

[3] Magdi K. Khair W. Addy Majewski. *Diesel Emissions and Their Control.* SAE International, 2006.

[4] Nikitidis Skaperdas Masoudi, Konstandopoulos, Evdoxia Kladopoulou Zarvalis, and Christodoulos Altiparmakis. Validation of a model and development of a simulator for predicting the pressure drop of diesel particulate filters. *SAE TECHNICAL PAPER SERIES*, 2001.

[5] DieselNet - Diesel Particulate Filters. "`https://www.dieselnet.com/`", 2011.

[6] Evangelos Skaperdas Eleni Papaioannou Dimitrios Zarvalis Athanasios G. Konstandopoulos, Margaritis Kostoglou and Evdoxia Kladopoulou. Fundamental studies of diesel particulate filters: Transient loading, regeneration and aging. *SAE International*, 2000.

[7] D. Sherwood M. Murtagh and L. Socha. Development of a diesel particulate filter composition and its effect on thermal durability and filtration performance. *SAE Technical Paper 940235*, 1994.

[8] N. Russo D. Fino S. Bensaid, D.L. Marchisio. Experimental investigation of soot deposition in diesel particulate filters. *Catalysis Today*, 147:295–300, 2009.

[9] Venkateswara Rao Bella R. Prasad. A review on diesel soot emission, its effect and control. *Chemical Reaction Engineering Catalysis,*, 5:69–86, 2010.

[10] Timothy Johnson. Vehicular emissions in review. *SAE Int. J. Engines*, 7(3):1207–1227, 2014.

[11] THE EUROPEAN PARLIAMENT AND THE COUNCIL OF THE EUROPEAN UNION. Directive (eu) 2016/2284, 4 December 2016.
`https://eur-lex.europa.eu/legal-content/IT/ALL/?uri=`
`CELEX:32016L2284`.

[12] Corning - Materials Science Technology and Innovation. ”`https://www.corning.com/`”.

[13] Shigeyuki Somiya. Handbook of advanced ceramics. 8.1:585–606, 2013.

[14] S. Bensaid, D. L. Marchisio, D. Fino, G. Saracco, and V. Specchia. Modelling of diesel particulate filtration in wall-flow traps. *Chemical Engineering Journal*, 154:211 – 218, 2009.

[15] M. Campolo J. Lupse and A. Soldati. Modelling soot deposition and monolith regeneration for optimal design of automotive dpfs. *Chemical Engineering Science*, 151:36–50, 2016.

[16] N. Vlachos A. Konstandopoulos, M. Kostoglou and E. Kladopoulou. Progress in diesel particulate filter simulation. *SAE Technical Paper*, 2005.

[17] S. Lorentzou A.G. Konstandopoulos, M. Kostoglou and N. Vlachos. Aspects of multifunctional diesel particulate filters and their efficient simulation. *Catalysis Today*, 188(1):2–13, 2012.

[18] Kazuhiro Yamamoto and Shinya Ohori. Simulations on flow and soot deposition in diesel particulate filters. *International Journal of Engine Research*, 14:333–340, 2013.

[19] Fabio Sbrizzai, Paolo Faraldi, and Alfredo Soldati. Appraisal of three-dimensional numerical simulation for sub-micron particle deposition in a micro-porous ceramic filter. *Chemical Engineering Science*, 60:6551 – 6563, 2005.

[20] J. Johnson A. Konstandopoulos. Wall-flow diesel particulate filters - their pressure drop and collection efficiency. *SAE Technical Paper*, 1989.

[21] J. Warren A. G. Konstandopoulos, E. Skaperdas and R. Allansson. Optimized filter design and selection criteria for continuously regenerating diesel particulate traps. *SAE Technical Paper*, page 12, 1999.

[22] A. G. Konstandopoulos adn M. Kostoglou. Analysis of asymmetric and variable cell geometry wall-flow particulate filters. *SAE International Journal of Fuels and Lubricants*, 7(2):489–495, 2014.

[23] Margaritis Kostoglou Toshiaki Shibata Yuki Hashizume Kazuki Nakamura, Athanasios Konstandopoulos. New asymmetric plugging layout of diesel particulate filters for the pressure drop reduction. *SAE Technical Pape*, 2014.

[24] M.Sahebi M.R. Ebrahimnataj, M.A.Ehteram and S.Abdolmaleki. Numerical and experimental study on the gaseous emission and back pressure during regeneration of diesel particulate filters. *Transportation Research Part D: Transport and Environment*, 62:11–26, 2018.

[25] Depcik C D and Hausmann A J. Review and a methodology to investigate the effects of monolithic channel geometry. *ASME J. Eng. Gas Turbines Power*, 135:032301, 2013.

[26] Athanasios G Konstandopoulos, Evangelos Skaperdas, and Mansour Masoudi. Microstructural properties of soot deposits in diesel particulate traps. *SAE Technical Paper*, 2002-01-1015:1 − 11, 2002.

[27] O. A. Haralampous G. C. Koltsakis, A. Konstantinou and Z. C. Samaras. Measurement and intra-layer modeling of soot density and permeability in wall-flow filters. *SAE Transactions - JOURNAL OF FUELS AND LUBRICANTS*, 115:90–102, 2006.

[28] Kentaro Iwasaki. Innovative aluminum titanate based - diesel particulate filter having asymmetric hexagonal cell geometry. *SAE Technical Papers*, 2012.

[29] W. S.-I. W. Salim H. A. Rahman S. H. Amirnordin, S. M. Seri and K. Hasnan. Pressure drop analysis of square and hexagonal cells and its effects on the performance of catalytic converters. *International Journal of Environmental Science and Development,*, 2(3), 2011.

[30] Housiada Konstandopoulos, Vlachos and Kostoglou. Simulation of triangular-cell-shaped, fibrous wall-flow filters. *SAE Technical Paper*, 2003.

[31] Eleni Papaioannou Athanasios G. Konstandopoulos. Update on the science and technology of diesel particulate filters. *KONA Powder and Particle Journal*, 26:36–65, 2008.

[32] Di Huang. *MODELING OF DIESEL PARTICULATE FILTER FILTRATION AND REGENERATION FOR TRANSIENT DRIVING SCHEDULES*. PhD dissertation, MICHIGAN TECHNOLOGICAL UNIVERSITY, 2011.

[33] James Clerc Arvind Harinath Yi Liu, Changsheng Su and Leigh Rogoski. Experimental and modeling study of ash impact on dpf backpressure and regeneration behaviors. *SAE Technical Paper*, 2015.

[34] Krishna Aravelli and Achim Heibel. Improved lifetime pressure drop management for robust cordierite (rc) filters with asymmetric cell technology (act). *Diesel Exhaust Emission Control*, 2007.

[35] K. Ohno K. Ogyu, T. Oya and A. Konstandopoulos. Improving of the filtration and regeneration performance by the sic-dpf with the layer coating of pm oxidation catalyst. *SAE TECHNICAL PAPER SERIES*, 2008.

[36] O. Yamanishi K. Tsuchimoto-K. Uoe T. Toma A. Nemoto, K. Iwasaki and H. Yoshino. Development of innovative diesel particulate filters based on aluminum titanate:design and validation. *SUMITOMO KAGAKU R&D Report*, 2011-II.